5-2016

Computational Fluid Dynamic Modeling of Natural Convection in Vertically Heated Rods

Mahesh Surendran
Utah State University

Recommended Citation

Surendran, Mahesh, "Computational Fluid Dynamic Modeling of Natural Convection in Vertically Heated Rods" (2016). *All Graduate Theses and Dissertations*. 5168.
https://digitalcommons.usu.edu/etd/5168

COMPUTATIONAL FLUID DYNAMIC MODELING OF NATURAL CONVECTION IN VERTICALLY HEATED RODS

by

Mahesh Surendran

A thesis submitted in partial fulfillment
of the requirements for the degree

of

MASTER OF SCIENCE

in

Mechanical Engineering

Approved:

Robert E. Spall, Ph.D. Major Professor	Barton L. Smith, Ph.D. Committee Member
Thomas H. Fronk, Ph.D. Committee Member	Mark R. McLellan, Ph.D. Vice President for Research and Dean of the School of Graduate Studies

UTAH STATE UNIVERSITY
Logan, Utah

2016

ABSTRACT

Computational Fluid Dynamic Modeling of Natural Convection in Vertically Heated Rods

by

Mahesh Surendran, Master of Science
Utah State University, 2016

Major Professor: Robert E. Spall, Ph.D.
Department: Mechanical and Aerospace Engineering

Natural convection is a phenomenon that occurs in a wide range of applications such as cooling towers, air conditioners, and power plants. Natural convection may be used in decay heat removal systems such as spent fuel casks, where the higher reliability inherent of natural convection is more desirable than forced convection. Passive systems, such as natural convection, may provide better safety, and hence have received much attention recently. Cooling of spent fuel rods is conventionally done using water as the coolant. However, it involves contaminating the water with radiation from the fuel rods. Contamination becomes dangerous and difficult for humans to handle. Further, the recent nuclear tragedy in Fukushima, Japan has taught us the dangers of contamination of water with nuclear radiation. Natural convection can perhaps significantly reduce the risk since it is self-sufficient and does not rely on other secondary system such as a blower as in cases of forced convection.

The Utah State University Experimental Fluid Dynamics lab has recently designed an experiment that models natural convection using heated rod bundles enclosed in a rectangular cavity. The data available from this experiment provides an opportunity to study and validate computational fluid dynamics (CFD) models. The validated CFD models can be used to study multiple configurations, boundary conditions, and changes in physics (natural and/or forced convection). The results are to be validated using experimental data such as the velocity field from particle image velocimetry (PIV), pressure drops across various sections of the geometry, and temperature distributions along the vertically heated rods. This research work involves modeling natural convection using two-layer turbulence models such as $k - \epsilon$ and RST (Reynolds stress transport) using both shear driven (Wolfstein) and buoyancy driven (Xu) near-wall formulations. The interpolation scheme employed is second-order upwinding using the general purpose code STAR-CCM+. The pressure velocity coupling is done using the SIMPLE method. It is ascertained that turbulence models with two-layer formulations are well suited for modeling natural convection. Further it is established that $k-\epsilon$ and Reynolds stress turbulence models with the buoyancy driven (Xu) formulation are able to accurately predict the flow rate and temperature distribution.

(70 pages)

PUBLIC ABSTRACT

Computational Fluid Dynamic Modeling of Natural Convection in Vertically Heated Rods

Mahesh Surendran

Spent fuel rods are conventionally stored in spent fuel pools for decades in order to contain the nuclear radiation. From the recent nuclear tragedy in Fukushima, Japan, we are aware of the danger of nuclear contamination. Leaving the spent fuel rods for a prolonged period of time with continuous heat transfer may cause damage to the containing structure and cause nuclear contamination. Buoyancy is phenomena in which fluid is caused to move around a heated source due to density differences. This phenomenon can be used in enhancing the heat transfer by placing the spent fuel rods in casks filled with helium gas. In doing so, the risk of structural damage due to thermal agitation may be significantly reduced. The physics involved in such phenomena are complex. This complicated physics in fluids can be modeled using high performance computers and a powerful numerical technique called computational fluid dynamics (CFD). However, the accuracy of the CFD simulations must be ascertained first. The accuracy of is determined by comparing the CFD simulation with experimental results.

The Experimental Fluid Dynamics Lab at Utah State University has recently designed an experiment that mimics the heat transfer around spent fuel rods using vertically heated rods enclosed in a rectangular cavity. The information available from this experiment can been used to study the accuracy of CFD simulations. Once the CFD simulation is validated using experimental data, they can be used to study various other similar geometric configurations and boundary conditions. The computer models are cost effective and time saving.

ACKNOWLEDGMENTS

I am deeply grateful to everyone who has offered their support during the course of my Master's program. I would particularly like to thank Dr. Robert Spall for his invaluable guidance and support, my parents Dr. S. Surendran and K.J. Jayalakshmy, my sister Aishwarya, and my friends for their support and faith.

I would also like to thank the United States Department of Energy's Nuclear Engineering University Program (grant 00128493) for funding this study.

Mahesh Surendran

CONTENTS

Page

ABSTRACT . . . iii

PUBLIC ABSTRACT . . . v

ACKNOWLEDGMENTS . . . vi

LIST OF TABLES . . . ix

LIST OF FIGURES . . . x

NOTATION . . . xii

ACRONYMS . . . xv

1 INTRODUCTION . . . 1
  1.1 Research Motivation . . . 1
  1.2 Literature Review . . . 1
  1.3 Experimental Configuration . . . 4

2 NUMERICAL METHOD . . . 6
  2.1 Computational Fluid Dynamics . . . 6
  2.2 Reynolds Averaged Navier-Stokes . . . 6
  2.3 Boussinesq Hypothesis . . . 7
  2.4 Turbulence Models . . . 9
    2.4.1 Spalart-Allmaras One-Equation Model . . . 10
    2.4.2 Standard $k-\epsilon$ Two-Equation Model . . . 12
    2.4.3 Realizable $k-\epsilon$ Two-Equation Model . . . 13
    2.4.4 Standard $k-\omega$ Two-Equation Model . . . 14
    2.4.5 Reynolds Stress Turbulence Seven-Equation Model . . . 16
  2.5 Near-Wall Turbulence . . . 18
  2.6 Calculation of Physical Properties . . . 21

3 NUMERICAL MODEL . . . 22
  3.1 Computational Domain . . . 22
  3.2 Mesh . . . 25
  3.3 Boundary Condition . . . 26

4 RESULTS . . . 28
  4.1 700 $\mathrm{W/m^2}$ Case . . . 28
  4.2 400 $\mathrm{W/m^2}$ Case . . . 36
  4.3 Grid Independence Study . . . 49

5 CONCLUSION . . . 52

REFERENCES 54

LIST OF TABLES

Table Page

2.1 Turbulence models. 9

2.2 Closure coefficients for Spalart-Allmaras model. 11

2.3 Closure coefficients for $k - \omega$ model. 16

2.4 Reference material properties. 21

3.1 Pressure loss coefficient. 27

4.1 Flow rates for 700 W/m^2 case. 29

4.2 Flow rates for 400 W/m^2 case. 41

4.3 Flow rate: grid independence study for $k - \epsilon$ Xu turbulence model. 49

4.4 Flow rate: grid independence study for RST Xu turbulence model. 50

LIST OF FIGURES

Figure Page

1.1 CAD model of experimental configuration. 4

3.1 Wind tunnel in vertically oriented configuration. 22

3.2 Horizontal view of the test section. 23

3.3 Conduits used for sending thermocouple wires. 24

3.4 Swirl elements on grid spacer. 24

3.5 Meshed view of the fluid domain. 25

3.6 Meshed view of the solid domain. 26

4.1 Temperature distribution on rods with various turbulence models for 700 W/m^2 case. 29

4.2 Axial variation of turbulent viscosity ratio. 30

4.3 Experimental vs. CFD velocity profile at x=0.0m, z=0.476m, 700 W/m^2. . . 31

4.4 Experimental vs. CFD velocity profile at x=0.0m, z=0.825m, 700 W/m^2. . . 32

4.5 Experimental vs. CFD velocity profile at x=0.0m, z=1.174m, 700 W/m^2. . . 32

4.6 Experimental vs. CFD velocity profile at x=0.0m, z=1.524m, 700 W/m^2. . . 33

4.7 Experimental vs. CFD velocity profile at x=-0.06m, z=0.476m, 700 W/m^2. 34

4.8 Experimental vs. CFD velocity profile at x=-0.06m, z=0.825m, 700 W/m^2. 34

4.9 Experimental vs. CFD velocity profile at x=-0.06m, z=1.174m, 700 W/m^2. 35

4.10 Experimental vs. CFD velocity profile at x=-0.06m, z=1.524m, 700 W/m^2. 35

4.11 Contour plot of velocity for $k-\epsilon$ Xu model; 700 W/m^2. 37

4.12 Contour plot of velocity for RST Xu model; 700 W/m^2. 38

4.13 Contour plot of normalized temperature for $k-\epsilon$ Xu model; 700 W/m^2. . . 39

4.14 Contour plot of normalized temperature for RST Xu model; 700 W/m^2. . . 40

4.15 Temperature distribution on rods with two turbulence models for the 400 W/m^2. 41

4.16 Experimental vs. CFD velocity profile at x=0.0m, z=0.476m, 400 W/m^2. . 42

4.17 Experimental vs. CFD velocity profile at x=0.0m, z=0.825m, 400 W/m^2. . 42

4.18 Experimental vs. CFD velocity profile at x=0.0m, z=1.174m, 400 W/m^2. . 43

4.19 Experimental vs. CFD velocity profile at x=0.0m, z=1.524m, 400 W/m^2. . 43

4.20 Experimental vs. CFD velocity profile at x=-0.06m, z=0.476m, 400 W/m^2. 44

4.21 Experimental vs. CFD velocity profile at x=-0.06m, z=0.825m, 400 W/m^2. 44

4.22 Experimental vs. CFD velocity profile at x=-0.06m, z=1.174m, 400 W/m^2. 45

4.23 Experimental vs. CFD velocity profile at x=-0.06m, z=1.524m, 400 W/m^2. 45

4.24 Contour plot of velocity for $k-\epsilon$ Xu model; 400 W/m^2. 46

4.25 Contour plot of velocity for RST Xu model; 400 W/m^2. 47

4.26 Contour plot of normalized temperature for $k-\epsilon$ Xu model; 400 W/m^2. . . 47

4.27 Contour plot of normalized temperature for RST Xu model; 400 W/m^2. . . 48

4.28 Temperature distribution: grid independent study for $k-\epsilon$ Xu turbulence model. 49

4.29 Temperature distribution :grid independence study for $k-\epsilon$ Xu turbulence model. 50

NOTATION

Variables

A	Cross-sectional area and anisotropic tensor
A_s	Surface area
D	Diameter
d	Distance from field point to nearest wall
Gr	Grashof number
h	Convective heat transfer coefficient
K	Temperature in kelvin
k	Thermal conductivity and turbulent kinetic energy
L	Characteristic length
l	Mixing length
$\dot{m}$	Mass flow rate
Nu	Nusselt number
Pr	Prandtl number
P_{abs}	Absolute pressure
P_{atm}	Atmospheric pressure
R	Regional gas constant
Re	Reynolds number
Ra	Raleigh number
S	Sutherland's constant
S_{ij}	Strain tensor
T_0	Reference temperature
T_s	Surface temperature
T_i	Turbulence intensity
T_∞	Ambient temperature
t	Time

u	x velocity component
$u(t)$	Instantaneous velocity
u_t	Frictional velocity
U_{ref}	Reference velocity
U_i	Mean component
u'_i	Fluctuating component
x_i	Vector component in index notation
$\overrightarrow{x}$	Vector
τ_w	Wall shear stress
α	Thermal diffusivity
β	Thermal expansion coefficient
ϵ	Turbulence dissipation
μ_0	Reference viscosity
μ	Dynamic viscosity
μ_t	Turbulent viscosity
ν_t	Eddy viscosity
ν	Kinematic viscosity
$\tilde{\nu}$	Eddy turbulent viscosity
ρ	Density
τ_{ij}	Reynolds stress tensor
Γ_t	Eddy diffusivity
Ω_{ij}	Rotational tensor
$\overline{\Omega}$	Mean rate of rotational tensor
ω_k	Angular velocity

Operations

$\frac{\partial}{\partial t}$	Derivative of time
$\frac{\partial}{\partial x_i}$	Derivative of component
∇	Gradient
$\nabla.$	Dot product
δ_{ij}	Kronecker delta
ϵ_{ijk}	Permutation tensor

ACRONYMS

CFD	Computational Fluid Dynamics
RANS	Reynolds Average Navier Stokes
$k-\epsilon$	k - epsilon
$k-\omega$	k - omega
RST	Reynolds Stress Turbulence Model
CAD	Computer Aided Design
NDT	Non Dimensional Temperature
SIMPLE	Semi-Implicit-Method for Pressure-Linked-Equation

CHAPTER 1

INTRODUCTION

1.1 Research Motivation

Natural convection is a phenomenon driven by buoyancy forces that are generated by a density difference due to temperature gradients. In such phenomena, the fluid surrounds the heat source; the heat is then diffused to the surrounding fluid, which causes density differences. The lighter, hotter fluid rises and is replaced by cooler, heavier fluid. This then becomes a continuous convective process and is generally called buoyancy driven flow. Natural convection is of great importance since it is present freely in nature and has many applications. In particular, natural convection around vertical and horizontal cylinders is of interest to the nuclear industry. The nature of the flow is affected by the shape, position, aspect ratio (height vs. diameter), and the type of encapsulation. Natural convection over single cylinder has been studied for decades, and recent studies have been extended to bundles and arrays enclosed in a cavity. This thesis aims at modeling natural convection for vertically heated rods. The effects that natural convection has on the vertically heated rods are studied through computational fluid dynamics (CFD). The solutions are compared with experimental studies conducted in the Experimental Fluid Dynamics lab at Utah State University by Jones [1].

1.2 Literature Review

The Reynolds number Eq. (1.1) represents the ratio of inertial force over viscous force. The Rayleigh number Eq. (1.2) represents the ratio of buoyancy force over viscous force. The Nusselt number Eq. (1.3) represents the ratio of convective heat transfer over conductive heat transfer. The Prandtl number Eq. (1.4) represents the ratio of viscous diffusion over thermal diffusion. The Grashof number Eq. (1.5) represents the ratio of buoyancy force over viscous force. These dimensionless numbers have significant importance in establishing the physics of the flow.

$$Re = \frac{\rho V d}{\mu} \tag{1.1}$$

$$Ra = \frac{g\beta}{\nu\alpha}(T_s - T_\infty)x^3 \tag{1.2}$$

$$Nu = \frac{hL}{k} \tag{1.3}$$

$$Pr = \frac{\nu}{\alpha} \tag{1.4}$$

$$Gr = \frac{Ra}{Pr} = \frac{g\beta(T_s - T_\infty)D^3}{\nu^2 s} \tag{1.5}$$

The Reynolds number can establish the importance of inertial and viscous resistance. Generally, for flows in smooth pipes with Reynolds number 2,300 or above suggests that the flow is fully turbulent. For natural convection, the fluid motion is not known beforehand; therefore, this dimensionless number cannot be used. In convective flows, where the flow is induced by buoyancy forces, the Rayleigh number is used to determine the nature of the flow. For flat plates, Rayleigh numbers over 10^9 suggest the flow is fully turbulent. The Nusselt number can suggest if heat transfer is primarily conductive or convective. Large values of the Nusselt number suggests the heat transfer is convective and turbulent, typically in the range of 100-1000. The Grashof number, which is similar to Raleigh number, is used in flows involving natural convection. For turbulent flows, the Grashof number is over 10^9.

From the literature survey conducted for this thesis, it is shown that there are several studies done in natural convection with numerous configurations; for example, vertical, horizontal, both with and without confinement. Nusselt [2] made a major contribution to the study of natural convection over a vertical cylinder. Contemporaries like Ackerman [3] have studied natural convection and validated Nusselt's theory. A major contribution is presented by Morgon [4] and Churchill and Chu [5], in which they both proposed time-averaged Nusselt number correlations.

Recently, Kuehn and Goldstein [6] and Farouk and Guceri [7] have conducted heat transfer analysis of natural convection around a single horizontal isothermal circular cylinder. They were able to report on the angular and radial velocity around the cylinder for Rayleigh numbers $<< 10^7$, and were also able to account for the local and area-averaged Nusselt number for a range of Prandlt numbers. Saitoh et al. [8] and Cesini et al. [9] conducted natural convection for horizontal cylinders. They have shown that heat transfer is a maximum at the bottom of the cylinder and is reduced vertically due to the influence of the thermal boundary layer thickness. Most research in this field has been limited to laminar convective flow. However, the motion of the buoyancy driven flow can also be turbulent. Turbulent flow may occur at Rayleigh number of 2×10^9 or more [4]. Kitamura et al. [10] investigated the effects of turbulence and its influences on the heat transfer around a horizontal cylinder, and found that the transitions occur for a Rayleigh number of 2.1×10^9. For Rayleigh numbers of 3.6×10^{13}, only the flow at the top of the cylinder is turbulent. Lieberman and Gebhart [11] and Marsters [12] conducted an investigation of natural convection for an array of heated cylinders, Yousefi and Ashjaee [13] investigated natural convection from a vertically aligned array of horizontal cylinders in which the effect of spacing and Rayleigh numbers on the heat transfer was investigated. It was discovered that the upper cylinders have reduced heat transfer relative to the lower cylinders. These studies have also shown that the spacing of the cylinders has an effect on the heat transfer. It further states that the temperature in the plume region is greater than the bulk fluid temperature. The plume region also has a forced convection effect on the upper cylinders in Lieberman and Gebhart [11]. Sparrow and Niethammer [14] studied free convection heat transfer for an array of two vertically separated cylinders in the range of Rayleigh numbers 2×10^4 to 2×10^5 with uniform wall temperature boundary conditions. Their study found that a gradual increase in the space between the cylinders increased the average Nusselt number.

A significant amount of numerical modeling of natural convection has been done in two-dimensions. For instance, Ghasmi et al. [15] modeled natural convection using a two-dimensional numerical model for different Rayleigh numbers. They concluded that an increase in Rayleigh number improves the natural convection flow and results in a reduction of heat source temperature. Most recently, Meng and Li [16] studied natural convection in horizontal cylinder filled with water based alumina nano fluid in three-dimensional model. Limited information about three-dimensional numerical modeling is available in the literature. However, since the last decade or two computational power has substantially increased, and it is now possible to develop robust three-dimensional CFD models of convective heat transfer.

1.3 Experimental Configuration

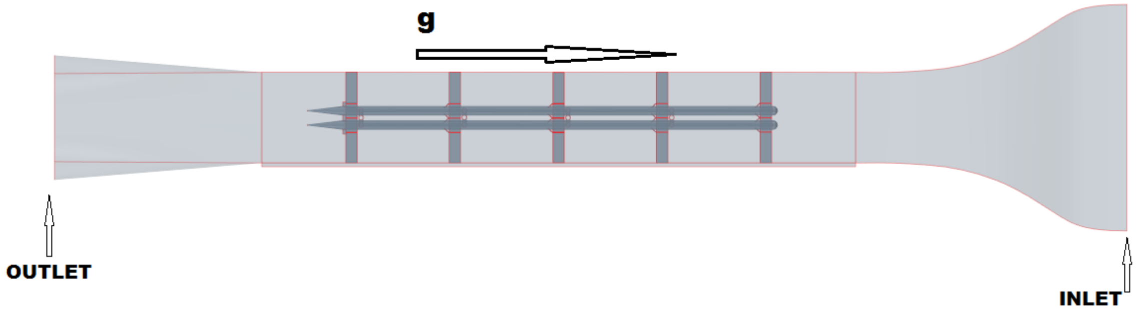

Fig. 1.1: CAD model of experimental configuration.

Fig. 1.1 is a CAD model of the geometric configuration in the Experimental Fluid Dynamics lab at Utah State University. The setup consists of four vertically positioned rods encapsulated inside a rectangular domain with a contraction at the inlet and an outlet transformation. More details about the experimental configuration are presented in Chapter 3. The benchmark studies by Jones [1] suggests that the Grashof number is $>> 2 \times 10^9$ at the vertical mid-point of the rods; therefore, the flow is assumed to be turbulent.

CHAPTER 2

NUMERICAL METHOD

2.1 Computational Fluid Dynamics

Computational fluid dynamics (CFD) is a numerical method used for the analysis of problems related to various physics such as fluid flow, heat transfer, combustion, and chemical reaction. CFD has a wide range of application in different fields such as aerospace, mechanical, nuclear, and chemical engineering. In CFD, the fluid is assumed to be a continuum. The finite volume approach is used to formulate the governing equations. Three important conservation equations must be satisfied to establish a CFD solution.

- Conservation of mass
- Conversation of momentum
- Conservation of energy

The governing equations are integrated over the control volume and discretized so that they form a system of algebraic equation, which can then be solved by a computer.

2.2 Reynolds Averaged Navier-Stokes

The Navier-Stokes equations are the most important in fluid mechanics, as these equations can mathematically describe the physics of fluid motion. However, analytical solutions for the Navier-Stokes equations are only available for very simple laminar flows. Most real life flows are turbulent and three-dimensional; hence an analytical solution may not be achievable. The Navier-Stokes equations can be solved using Direct Numerical Simulation (DNS), which solves Navier-Stokes equations as is; however, it would require extensive computational resources and time, and this is not a feasible approach in general. Reynolds-Averaged Navier-Stokes (RANS) are time-averaged equations of motion for fluid flow. The idea is to decompose turbulence into two components, which are the mean and fluctuating components. This is called Reynolds decomposition.

$$u_i(\overrightarrow{x},t) = U_i(\overrightarrow{x}) + u_i'(\overrightarrow{x},t) \tag{2.1}$$

Here u_i is the velocity at any instant, U_i is the mean component, and u_i' is the fluctuating component. The Navier-Stokes equations are averaged using Eq. (2.1). In general, there are time-averaged as well as ensemble averaged approaches. The former is used for steady state flows (flows which are time independent) and the latter for transient flows (flows which are time dependent).

$$\rho\frac{\partial u_i}{\partial t} + \rho\bar{u}_j\frac{\partial u_i}{\partial x_i} = \rho\overline{f}_i + \frac{\partial}{\partial x_j}\left[-\bar{p}\delta_{ij} + \mu\left(\frac{\partial \bar{u}_i}{\partial x_j} + \frac{\partial \bar{u}_j}{\partial x_i}\right) - \rho\overline{u_i'u_j'}\right] \tag{2.2}$$

The RANS equation are given by Eq. (2.2) for an incompressible Newtonian fluid written in index notation. The Reynolds averaging results in additional terms in the equation and these terms are called the Reynolds stresses.

$$\tau_{ij} = -\rho\overline{u_i'u_j'} \tag{2.3}$$

In order to close the system, the components of the Eq. (2.3) must be solved. Generally, this is known as the turbulence closure problem. An ideal turbulence model should be capable of being applied to a wide range of problems, it should have reasonable accuracy, and must be computationally inexpensive. Some simplifications must be done to the Reynolds stresses in order to incorporate two-equation models.

2.3 Boussinesq Hypothesis

The Boussinesq hypothesis (note that this is not related to Boussinesq approximation used for simplification of free-convection flows) is a widely used simplification used to obtain two-equation turbulence models. It hypothesizes that the momentum transfer, due to turbulent eddies, can be modeled using an "eddy viscosity." For an incompressible flow, the

Reynolds stresses can be modeled using the following equation,

$$\rho \tau_{ij} = \mu_t \left[\frac{\partial U_i}{\partial x_j} + \frac{\partial U_j}{\partial x_i} \right] - \frac{2}{3} \delta_{ij} \rho k, \tag{2.4}$$

where k is the turbulent kinetic energy per unit mass, μ_t is the eddy viscosity and U_i is the mean velocity component. Using the Boussinesq hypothesis, the six Reynolds stresses are reduced to two unknowns, μ_t and k. This is established by defining the turbulent kinetic energy k as,

$$k = \frac{1}{2} \overline{u_i' u_j'}. \tag{2.5}$$

The average root mean square velocities divided by the reference mean velocities defines the turbulent kinetic energy T_i.

$$T_i = \frac{\frac{2}{3} k^{1/2}}{U_{ref}} \tag{2.6}$$

By specifying the turbulence intensity, the turbulent kinetic energy per unit mass can be ascertained. The specification of the turbulence intensity is based on how intense the turbulence is. Turbulence transport of scalar quantities such as mass, density etc. can also be modeled similarly, as show in Eq. (2.7),

$$-\rho \overline{u_i' \varphi'} = \Gamma_t \frac{\partial \Phi}{\partial x_i} \tag{2.7}$$

where Γ_t is the eddy diffusivity. Both momentum turbulence transport as well as scalar transport modeling of turbulence is done using similar procedure; therefore, the eddy diffusivity Γ_t and turbulent viscosity μ_t are nearly equal. Two-equation turbulence models are widely used in the industry and academia. The Boussinesq hypothesis is generally used by all commercial and open source CFD solvers.

2.4 Turbulence Models

The selection of turbulence models is based on availability in the commercial software STAR-CCM+ [17]. Models ranging from one-equation (Spalart-Allmaras) to seven-equation models (RST) are available in STAR-CCM+, see Table 2.1. The one-equation model is of particular interest to the aerospace industry as it is one of the simplest turbulence models and is computationally economical. The $k-\epsilon$ and $k-\omega$ turbulence models are widely used and popular in industry because their relative accuracy, for being economic, and widely validated for numerous problems by both industry and academia. Modifications to the two-equation models are employed for solving flows involving low Reynolds number flows and transitional flows. The RST models are not as widely used as the two-equation models in industry since they are computationally expensive and not as well validated as the $k-\epsilon$ and $k-\omega$ models. However, recently the RST models have received renewed interest since the computational power has increased exponentially.

For modeling natural convection, two-equation models with a two-layer formulation are of particular interest. This approach was first put forth by Rodi [18]. The method divides the viscous sub-layer into two parts. The dissipation rate ϵ and turbulent viscosity μ_t are specified as functions of wall distance. The $k-\epsilon$ and RSM models with two-layer formulations are the focus for this thesis work. Two-layer formulations using buoyancy driven [19] and shear driven [20] near-wall approaches are studied in detail to assess the steady state temperature distributions on the rods. The turbulence models used are shown in Table 2.1.

Table 2.1: Turbulence models.

No. of Equations	Turbulence Model
One	Spalart-Allamaras
Two	$k-\epsilon$
Two	$k-\omega$
Seven	RST

2.4.1 Spalart-Allmaras One-Equation Model

The Spalart-Allmaras turbulence model is a one-equation turbulence model. This model solves a transport equation for the eddy turbulent viscosity [21]. The model is specialized for applications in the aerospace industry and is suitable for solving problems with adverse pressure gradients in the boundary layer. Recently, this model has also been used for solving problems involving internal fluid flow in turbo-machines. However, this model is generally not suitable for low Reynolds number flows. The Spalart-Allmaras turbulence model solves transport equation for a viscosity like variable $\tilde{\nu}$ given as,

$$\frac{\partial \tilde{\nu}}{\partial t}+\mu_j \frac{\tilde{\nu}}{\partial x_j} = C_{b1}\left[1-f_{t2}\right]\tilde{S}\tilde{\nu}+\frac{1}{\sigma}\{\nabla.\left[(\nu+\tilde{\nu})\nabla\tilde{\nu}+C_{b2}|\nabla\nu|^2\right]\}-\left[C_{w1fw}-\frac{C_{b1}}{\kappa^2}f_{t2}\right](\frac{\tilde{\nu}}{d})^2+f_{t1}\Delta U^2 \tag{2.8}$$

where the turbulent eddy viscosity is computed as,

$$\nu_t = \tilde{\nu} f_{u1} \quad f_{u1} = \frac{\varkappa^3}{\varkappa^3 + C_{\mu 1}^3} \quad \varkappa = \frac{\tilde{\nu}}{\nu}. \tag{2.9}$$

The other terms in the equation are,

$$\tilde{S} \equiv S + \frac{\tilde{\nu}}{\kappa^2 d^2} f_{u2} \quad f_{u2} = 1 - \frac{\varkappa}{1+\varkappa f_{u1}} \tag{2.10}$$

$$f_w = g\left[\frac{1+C_{w3}^6}{g^6+C_{w3}^6}\right]^{1/6} \qquad g = r + C_{w2}(r^6 - r) \quad r \equiv \frac{\tilde{\nu}}{\tilde{S}\kappa^2 d^2} \tag{2.11}$$

$$f_{t1} = C_{t1} g_t \exp\left(-C_{t2}\frac{\omega_t^2}{\Delta U^2}\left[d^2 + g_t^2 d_t^2\right]\right) \tag{2.12}$$

$$f_{t2} = C_{t3}\exp(-C_{t4}\varkappa^2) \tag{2.13}$$

$$S = \sqrt{2\Omega_{ij}\Omega_{ij}}. \tag{2.14}$$

Here, Ω_{ij} is the rotational tensor and is defined as

$$\Omega_{ij} = \frac{1}{2}\left(\frac{\partial u_i}{\partial u_j} - \frac{\partial u_j}{\partial x_i}\right) \tag{2.15}$$

Eq. (2.8) represents the transport equation where d is the distance from the closest surface and ΔU^2 is the normal of the difference between the velocity at the tip of the field and the field point. The closure coefficients are summarized in Table 2.2.

Table 2.2: Closure coefficients for Spalart-Allmaras model.

coefficients	value
σ	2/3
C_{b1}	0.1355
κ	0.41
C_{w1}	$C_{b1}/\kappa^2 + (1 + C_{b2})/\sigma$
C_{w2}	0.3
C_{w3}	2
C_{v1}	7.1
C_{t1}	1
C_{t2}	2
C_{t3}	1.1
C_{t4}	2

2.4.2 Standard $k - \epsilon$ Two-Equation Model

The $k - \epsilon$ model is one of the most widely used turbulence models in industry as well as academia. Its popularity can be attributed mainly to it being computationally inexpensive and being widely validated. Launder and Spalding [22] proposed this model in 1972. Applying the Boussinesq hypothesis to the Reynolds stress terms, two additional transport equations must be solved to close the system. These equations determine the turbulent kinetic energy k and turbulent dissipation ϵ. For an incompressible flow, Eq. (2.16) describes the transport equation for the turbulent kinetic energy.

$$\frac{\partial}{\partial t}(k) + \frac{\partial}{\partial x_i}(kU_i) = \frac{\partial}{\partial x_i}\left[\left(\nu + \frac{\nu_t}{\sigma_k}\right)\frac{\partial k}{\partial x_i}\right] + G - \epsilon \tag{2.16}$$

Eq. (2.17) is the transport equation for turbulent dissipation rate where, G (Eq.2.18) represents the generation of turbulent kinetic energy due to mean velocity gradients. The coefficients for the Eq. (2.16) and Eq. (2.17) are $C_{\epsilon 1} = 1.44$, $C_{\epsilon 2} = 1.92$, $\sigma_k = 1.0$, and $\sigma_\epsilon = 1.3$.

$$\frac{\partial}{\partial t}(\epsilon) + \frac{\partial}{\partial x_i}(\epsilon U_i) = \frac{\partial}{\partial x_i}\left[\left(\nu + \frac{\nu_t}{\sigma_k}\right)\frac{\partial \epsilon}{\partial x_i}\right] + C_{\epsilon 1}\frac{\epsilon}{k}G - C_{\epsilon 2}\frac{\epsilon^2}{k} \tag{2.17}$$

$$G = 2\mu_t S_{ij} S_{ji}. \tag{2.18}$$

Here, S_{ij} is the strain tensor defined as

$$S_{ij} = \frac{1}{2}\left[\frac{\partial U_i}{\partial x_j} + \frac{\partial U_j}{\partial x_i}\right]. \tag{2.19}$$

The eddy viscosity is calculated from the following relation,

$$\nu_t = C_\mu \frac{k^2}{\epsilon} \tag{2.20}$$

where $C_\mu = 0.09$

The coefficients used in the Eq. (2.17), (2.19), and (2.20) have been ascertained empirically over the years using air and water. They are generally valid for most other fluids [23]. These constants are usually left at default values.

2.4.3 Realizable $k - \epsilon$ Two-Equation Model

The realizable $k - \epsilon$ model is a modified version of the standard $k - \epsilon$ model, proposed by Shih [24]. This modified version can capture physics that involves flow separation and recirculation, boundary layers under strong adverse pressure gradients, flows involving rotation, etc.

The k transport equation for both standard and realizable models are identical (Eq.2.16). The significant difference is in modeling the turbulent dissipation ϵ as given by Eq. (2.21).

$$\frac{\partial}{\partial t}(\epsilon) + \frac{\partial}{\partial x_i}(\epsilon U_i) = \frac{\partial}{\partial x_i}\left[\left(\nu + \frac{\nu_t}{\sigma_k}\right)\frac{\partial \epsilon}{\partial x_i}\right] + C_{\epsilon 1} S \epsilon - C_{\epsilon 2}\frac{\epsilon^2}{k + \sqrt{\nu\epsilon}} \tag{2.21}$$

Here,

$$C_{\epsilon 1} = \max\left[0.43, \frac{\eta}{\eta + 5}\right] \tag{2.22}$$

where,

$$\eta = S\frac{k}{\epsilon} \tag{2.23}$$

and

$$S = \sqrt{2S_{ij}S_{ji}}. \tag{2.24}$$

The eddy viscosity is calculated similar to the standard $k - \epsilon$ approach and is given by Eq. (2.25).

$$\nu_t = C_\mu \frac{k^2}{\epsilon}. \tag{2.25}$$

However, C_μ is not a constant. It is defined as,

$$C_\mu = \frac{1}{A_0 + A_s \frac{kU^*}{\epsilon}} \tag{2.26}$$

where,

$$U^* = \sqrt{S_{ij}S_{ij} + \tilde{\Omega_{ij}}\tilde{\Omega_{ij}}} \tag{2.27}$$

and

$$\tilde{\Omega_{ij}} = \overline{\Omega_{ij}} - \epsilon_{ijk}\omega_k. \tag{2.28}$$

The variable $\tilde{\Omega_{ij}}$ is the mean rate of rotation tensor with angular velocity ω_k and the permutation tensor ϵ_{ijk}. The closure coefficients are given as

$$A_0 = 4.04, A_S = \sqrt{6}\cos(\phi) \tag{2.29}$$

where,

$$\phi = \frac{1}{3}\cos^{-1}\left[\sqrt{6}\frac{S_{ij}S_{ji}S_{ki}}{(S_{ij}S_{ij})^{3/2}}\right]. \tag{2.30}$$

2.4.4 Standard $k-\omega$ Two-Equation Model

Kolmogrov (1942) proposed the original $k-\omega$ model with k as turbulent kinetic energy and ω as the dissipation rate. Over the years several modifications have been made to the original model by Saffman [25], Launder and Spalding [26] and Wilcox [27]. The Wilcox $k-\omega$ model has incorporated modification for low Reynolds number, compressibility, and shear flow spreading.

The k in this turbulence model the is same as that of the standard $k-\epsilon$ model (2.16). However, $\sigma_k = 2.0$ and ϵ is defined as,

$$\epsilon = \beta^* f_{\beta^*} k\omega. \tag{2.31}$$

For incompressible flow, f_{β^*} has the following function,

$$f_\beta^* = \begin{cases} 1 & \varkappa_k \geq 0 \\ \frac{1+68\varkappa_k^2}{1+400\varkappa_k^2} & \varkappa_k \gtrsim 0 \end{cases} \tag{2.32}$$

where,

$$\varkappa_k = \frac{1}{\omega^3}\frac{\partial k}{\partial x_j}\frac{\partial \omega}{\partial x_j} \tag{2.33}$$

$$\beta^* = \beta^*_\infty \left[\frac{4/15 + (Re_t/R_k)^4}{1 + (Re_t/R_k)^4}\right] \tag{2.34}$$

$$Re_t = \frac{k}{\nu\omega}. \tag{2.35}$$

The specific dissipation rate ϵ is where $k - \omega$ models incorporate detailed changes in comparison with the $k - \epsilon$ model. The ϵ transport equation is given as

$$\frac{\partial}{\partial t}(\epsilon) + \frac{\partial}{\partial x_i}(\epsilon U_i) = \frac{\partial}{\partial x_i}\left[\left(\nu + \frac{\nu_t}{\sigma_k}\right)\frac{\partial \epsilon}{\partial x_i}\right] + \alpha\frac{\omega}{k}G - \beta f_\beta \omega^2 \tag{2.36}$$

where,

$$\alpha = \frac{\alpha_\infty}{\alpha^*}\left[\frac{\alpha_0 + Re_t/R_\omega}{1 + Re_t/R_\omega}\right] \tag{2.37}$$

$$\alpha^* = \alpha^*_\infty \left[\frac{\beta/3 + Re_t/R_k}{1 + Re_t/R_k}\right] \tag{2.38}$$

and

$$f_\beta = \frac{1 + 70\varkappa_\omega}{1 + 80\varkappa_\omega} \quad \varkappa_\omega = |\frac{\Omega_{ij}\Omega_{jk}S_{ki}}{(\beta^*_\infty \omega)^3}|. \tag{2.39}$$

Here Ω_{ij} is the mean rotation tensor,

$$\Omega_{ij} = \frac{1}{2}\left[\frac{\partial U_i}{\partial x_j} - \frac{\partial U_j}{\partial x_i}\right]. \tag{2.40}$$

The turbulent viscosity is defined as

$$\nu_t = \alpha^* \frac{k}{\omega}. \tag{2.41}$$

The closure coefficients are summarized in Table 2.3.

Table 2.3: Closure coefficients for $k - \omega$ model.

coefficients	value
α^*_∞	1
α_∞	0.52
α_0	$\frac{1}{9}$
$\beta*_\infty$	0.09
β	0.072
R_β	8
R_k	6
R_ω	2.95
σ_k	2.0
σ_ω	2.0

2.4.5 Reynolds Stress Turbulence Seven-Equation Model

The RST model is the most computationally intensive RANS model. It is also known as Differential Reynolds Stress (DRS) Model. The RST model does not assume the Boussinesq hypothesis. Rather, this model solves the RANS equation without any simplification of the Reynolds stresses (Eq.2.42) and was first reported by Launders in 1975 [28].

$$\tau_{ij} = -\rho\overline{u'_i u'_j} \tag{2.42}$$

Transport equation for τ_{ij} and ϵ are solved to close the system.

The RST model also requires significantly more iterations than the one-equation and two-equation turbulence models to converge. This could be due to the mathematical stiffness of RST model. The RST model is effective in comparison with two-equations models when the flow involves physics and that which are dominated by streamline curvature and rotational effects. The general RST model can be found in [28], and the STAR-CCM+ implementation can be found in [17].

For a two-layer model, the first four coefficients are expressed in terms of the turbulent Reynolds number as recommended by Launders and Shima [29],

$$C_1 = 1 + 2.58 a a_2^{\frac{1}{4}} \{1 - \exp\left[(-0.0067 Re_t)^2\right]\} \quad Re_t = \frac{k^2}{\epsilon v} \tag{2.43}$$

$$C_2 = 0.75\sqrt{a}, \tag{2.44}$$

$$C_{1w} = -\frac{2}{3}C = 1 + 1.67, \tag{2.45}$$

$$C_{1w} = -\frac{2}{3}C = 1 + 1.67, \tag{2.46}$$

$$C_{2w} = \max\left[\frac{4C_2 - 1}{6C_2}, 0\right] \tag{2.47}$$

where the parameter a and tensor invariant $a2$ and $a3$ are defined as,

$$a = 1 - \frac{9}{8}(a_2 - a_3), a_2 = A : A, a_3 = A_{ij}A_{kj}A_{ji} \tag{2.48}$$

where the anisotropic tensor A is defined as,

$$A = \frac{R}{k} - \frac{2}{3}I. \tag{2.49}$$

2.5 Near-Wall Turbulence

The walls in the geometry present a different problem while modeling turbulence. In the presence of a wall with a no-slip condition, the flow is reduced to laminar owing to the viscous effects. The velocity near the wall changes rapidly within a small distance. For high speed flows, the boundary layer is very thin, and in order to capture the effects of the boundary layer, many nodes may be required. This will result in an expensive computation. The appropriate selection of a wall treatment is hence essential for correct modeling of the physics.

There are several ways to model the near-wall turbulence. In STAR-CCM+ there are three approaches for wall treatment; low-wall y^+, high-wall y^+, and all-wall y^+. The inner region on the boundary layer is split into three layers; viscous, log-law, and buffer layers.

In the low-wall y^+ method, wall treatment requires no modification in the viscous region and the governing equations are integrated up to the wall. This means that finer cells are required at the near wall region to accurately model the physics. For high Reynolds number flows this method can be expensive since the boundary layer is very thin with a high velocity gradient, which requires several cells near the wall to capture the physics. This treatment is suitable for low Reynolds-number-flows with a thicker boundary layer. In order to maintain this condition, the wall y^+ must be maintained near 1.

In the high-wall y^+ wall treatment, the viscous layer requires some modification. Wall functions are used to model the physics in the viscous layer. The wall shear stress, turbulent production and turbulent dissipation are derived using the boundary layer theory. This treatment assumes that the near wall cell lies in the log-law region of the boundary layer with $y^+ > 30$. This approach significantly reduces the computation for high Reynolds number flow.

The all-wall y^+ wall treatment is a combination of both low and high-wall y^+ treatment. When the cell falls in the buffer layer, a blending function is used to calculate the turbulent quantities. This treatment is used for complex geometries with relatively low and high mesh resolution near wall. In some cases, with complicated geometries, it may be difficult to achieve a mesh with a reasonable resolution everywhere along the wall; therefore, the all-wall y^+ approach is a good remedy for such geometries.

The definition for y^+, frictional velocity u_t, and wall shear stress τ_w are,

$$y^+ = \frac{u_t\sqrt{y}}{\nu} \tag{2.50}$$

where,

$$u_t = \sqrt{\tau_w/\rho} \tag{2.51}$$

and

$$\tau_w = \mu\frac{\partial u}{\partial y}|_{wall}. \tag{2.52}$$

The two-layer approach suggested by Rodi [18] is an alternative to model low Reynolds number flow. Here, in the two-layer approach the turbulence model is coupled with a one-equation model. The turbulent dissipation ϵ and turbulent viscosity μ_t are specified as function of wall distance. The ϵ specified near the wall blends with values computed from the transport equation far from the wall.

The dissipation rate near the wall is computed as,

$$\epsilon = \frac{k^{3/2}}{l_\epsilon} \tag{2.53}$$

Two two-layer one-equation models are studied; those by Wolfstein [20] and Xu [19]. The Wolfstein model is recommended primarily for modeling shear driven flows and the Xu model for buoyancy driven flows.

The one-equation Wolfstein model is,

$$l_\epsilon = c_l y\left[1 - \exp\left(-\frac{Re_y}{A_\epsilon}\right)\right] \tag{2.54}$$

where, $A_\epsilon = 2c_l$ and $c_l = kC_\mu^{-3/4}$, $C_\mu = 0.09$, and $k = 0.42$. The turbulent viscosity is calculated from the following,

$$\frac{\mu_t}{\mu} = Re_y C_\mu^{(1/4)} k \left[1 - \exp\left(-\frac{Re_y}{A_\mu}\right)\right]. \tag{2.55}$$

The one-equation Xu model is,

$$l_\epsilon = \frac{8.8y}{1 + 10/y_v^* + 5.15 \times 10^{-2} y_v^*} \frac{1}{\sqrt{v^2/k}} \tag{2.56}$$

where,

$$\overline{v^2}/k = 7.19 \times 10^3 Re_y - 4.33 \times 10^-5 Re_y^2 + 8.8 \times 10^-8 Re_y^3 \tag{2.57}$$

and

$$y_\nu^* = Re_y \sqrt{v^2/k}. \tag{2.58}$$

The two-layer models are computationally more expensive than wall functions, yet it must be employed since near-wall resolution is imperative for natural convection. Accurate prediction of near-wall physics is the key for accurate modeling of natural convection since the heat transfer from the wall is what actually drives the flow. The two-layer approach is incorporated into the $k - \epsilon$ model and linear pressure strain RST model. Other turbulence models investigated in this thesis employ either low-wall y^+ or all-wall y^+ treatments. Consequently, the wall y^+ is maintained at approximately 1 throughout the heat transfer surfaces. In STAR-CCM+, the two-layer approach can also be modeled with all-wall y^+ treatment. Some of the regions in the geometry may not have been meshed with such high resolution at near the wall. The all-wall y^+ functionality in the software mitigates the problem by switching to wall functions.

2.6 Calculation of Physical Properties

The density is calculated using incompressible ideal gas law (Eq.2.59), which is a function of temperature and pressure. This is defined as,

$$\rho = \frac{p_{abs}}{RT} \tag{2.59}$$

where, ρ is the density, p_{abs} is the absolute reference pressure, R is the universal gas constant, and T is temperature.

The viscosity is calculated using Sutherland's law (Eq.2.60) where, T_0 and μ_0 are reference temperature and viscosity respectively. S is Sutherland's constant. The thermal conductivity for air is calculated using a linear fit between 100K to 1000K. The reference values are set as show in Table 2.4.

$$\frac{\mu}{\mu_0} = \left(\frac{T}{T_0}\right)^{3/2} \left(\frac{T_0 + S}{T + S}\right) \tag{2.60}$$

Table 2.4: Reference material properties.

Property	Value
Density	1.0289 Kg/m^3
Pressure	86529 Pa
Temperature	293 K

CHAPTER 3

NUMERICAL MODEL

3.1 Computational Domain

Fig. 3.1: Wind tunnel in vertically oriented configuration.

Fig. 3.1 is a representation of the wind tunnel in the Experimental Fluid Dynamics lab at Utah State University from Jones [1]. It is set up in a manner such that the test section can be configured vertically or horizontally and also in various orientation in z axis. For natural convection, a vertical configuration is used. The computational domain consists of an inlet contraction, test section, and outlet transformation. The test section contains four vertical rods. These rods are held at their positions by grid spacers. Five grid spacers are used in the test section.

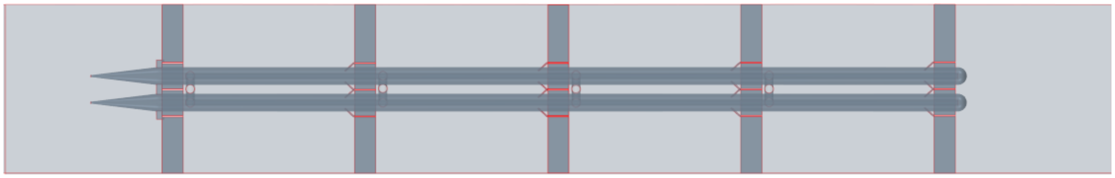

Fig. 3.2: Horizontal view of the test section.

The test section is two meters with a cross-sectional area of 304.8 × 304.8 millimeters, as shown in Fig. 3.2 these dimensions are not shown in the figure. One of the four walls is constructed with aluminum 6061-T6 plate which is included in the numerical model. The rods are 1.58 meters long with an inner and outer diameter of 0.00952 meters and 0.3175 meters respectively. The rods are also made of aluminum 6016-T6 material.

The rods shown in Fig. 3.2 are heated using thermocouple wires. These wires are sent into the test section through conduits as shown in Fig. 3.3. The computational geometry also consists of hangers present downstream of the domain near the last grid spacer.

The first four of the grid spacers are integrated with the swirl vanes as shown in Fig. 3.4, however the fifth one is left out. The presence of these swirl vanes have eliminated symmetry inherent in the base geometry. The swirl vane elements are employed with an intention to increase the interaction of the fluid with the rods to improve heat transfer.

The computational domain is split into solid and fluid domains. The solid domain

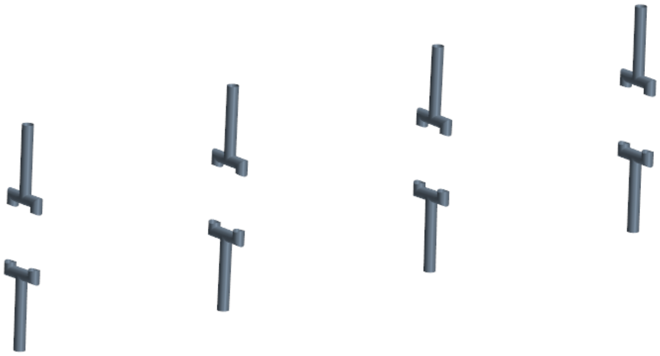

Fig. 3.3: Conduits used for sending thermocouple wires.

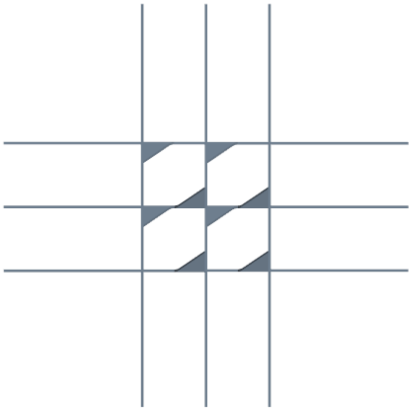

Fig. 3.4: Swirl elements on grid spacer.

mainly consists of the rods and the aluminum plate, while the fluid domain is essentially the test section, contraction, gird spacers, hangers, conduits, and outlet transformation.

3.2 Mesh

Splitting the computational domain into smaller, finite volumes is called meshing. This is done using the meshing module available in the commercial software STAR-CCM+ [17].

The fluid domain is meshed using the trimmed mesher and is an unstructured scheme that uses hexahedral elements. The trimmed mesher is suitable for geometries that are complex. Structured prism layers are also modeled along with the trimmed mesher to resolve the boundary layer with wall y^+ maintained at approximately 1. Fig. 3.5 is a view of the fluid domain. Special attention is given to conduits and grids spacers with swirl vanes. The mesh is refined at these locations. The meshed region downstream of the grid spacers is also refined since capturing the physics here is essential.

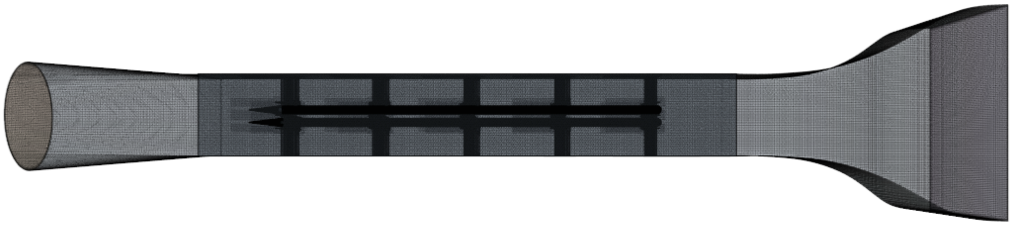

Fig. 3.5: Meshed view of the fluid domain.

The solid domain shown in Fig.3.6 is meshed using the unstructured polyhedral elements which reduce the cell count in the domain significantly. The solid domain is relatively smaller than the fluid domain and only models diffusion, hence the meshing requirement is significantly less.

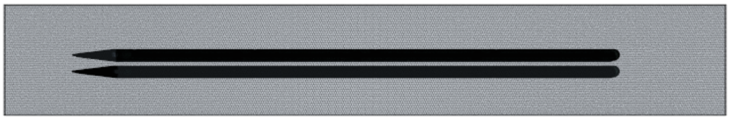

Fig. 3.6: Meshed view of the solid domain.

The solid and the fluid domains are not mapped conformally, i.e., they have no connectivity between the meshes. The interface module in STAR-CCM+ is used to calculate the interaction between the solid and fluid domains.

3.3 Boundary Condition

The boundary conditions are specified similar to that of the experimental setup. A heat flux boundary condition of 2333 W/m^2 is specified in the inner surface of the rods, which is equivalent to specifying 700 W/m^2 at the outer surface. Similarly, for second case 1335 W/m^2 is specified at the inner surface, which is equivalent to 400 W/m^2 in the outer surface. It must be noted that the heat flux boundary condition is not uniform throughout the surfaces as there are sections where there is zero heat flux. This non uniform heat flux boundary condition is implemented using the field functions. The reference temperature is set at 293 K, and the reference pressure is set at 86529 Pa. A stagnation inlet is specified at the inlet. To take into account the pressure drop due to the flow straighteners present at the inlet, a pressure loss coefficient is specified at the inlet using Bernoulli's equation. The pressure loss is specified as show in Table 3.1 from Jones [1].

Table 3.1: Pressure loss coefficient.

Case W/m^2	Coefficient
400	233 ± 56
700	160 ± 35

The boundary condition at the outlet is specified as a pressure outlet. The walls throughout were specified as adiabatic with a no-slip condition. The turbulence intensity is specified as 1 percent and turbulent viscosity ratio as 10.

Interpolation schemes consist of second-order upwinding for the convective terms and the second-order central difference for the diffusion terms. The pressure velocity coupling is achieved using the SIMPLE method. Initial guesses are used for initializing the numerical model. An accurate value can help in speeding convergence. Therefore, the temperature in the solid region is set to 360K initially and z-velocity in fluid domain is set to 0.15 m/s. Under relaxations were set adequately low in order to assist convergence.

CHAPTER 4

RESULTS

The results from two cases are presented here. The first with a heat flux boundary condition of 700 W/m^2 and the second with a heat flux boundary condition of 400 W/m^2. The first case is studied in greater detail than the second as it was discovered from the former that some of the turbulence models do not accurately model the relevant physics. Therefore, they are excluded from consideration for the second case. In the computational procedure, residuals were driven down to 10^{-3} or lower in steady state for all cases, except the $k - \omega$. The $k - \omega$ results are excluded from comparison with experimental data since those runs did not sufficiently converge; however, a steady mass flow rate was achieved. For the 400 W/m^2 case, only the $k - \epsilon$ and RST turbulence models with Xu near-wall formulation are studied. A grid independence study using the $k - \epsilon$ and RST turbulence models with Xu near-wall formulation is also presented later in this chapter.

4.1 700 W/m^2 Case

The flow rates for the different turbulence models are compared with the experimental study of Jones [1]. The temperature distribution along two of the rods is presented and compared with the experimental results. Experimental velocity profiles at eight different locations are also compared with different turbulence model results. The performance of the turbulence models with two-layer formulations is also compared. Various contour plots of velocity and temperature are presented. Approximately 8 million cells are used for each of the simulations. This is proven to be sufficient from a grid independence study which is discussed later in this chapter.

From Table 4.1 it is clear that the flow rates from CFD solution of the Spalart-Allmaras and $k - \omega$ turbulence models do not correlate well with the experimental data. All other models with two-layer formulations have a better agreement with the experimental result;

Table 4.1: Flow rates for 700 W/m^2 case.

Turbulence Model	CFD kg/s	Exp kg/s
Spalart-Allmaras	0.0188	0.025
Standard $k-\epsilon$, Xu	0.0287	0.025
Realizable $k-\epsilon$,Xu	0.0257	0.025
Realizable $k-\epsilon$, Wolf	0.0202	0.025
RST, Xu	0.0273	0.025
RST, Wolf	0.0236	0.025
$k-\omega$	0.0138	0.025

notably realizable $k-\epsilon$ model has the strongest correlation. However the standard $k-\epsilon$ model seems to slightly over estimate the flow rate. Since the two-layer models are suitable for flows requiring high near wall resolution, they often show better agreement with the experimental data. The pressure loss coefficient of $K = 166$ specified at inlet leads to results that agree with the experimental mass flow rate for all models except the Spalart-Allmaras and $k-\omega$.

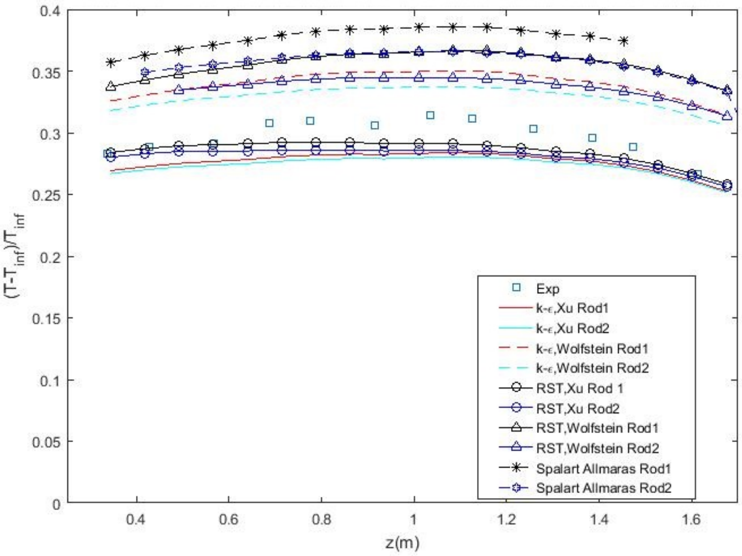

Fig. 4.1: Temperature distribution on rods with various turbulence models for 700 W/m^2 case.

The plot in Fig. 4.1 is a plot of dimensionless temperature as a function of distance along the streamwise direction on the rod walls. The temperature distribution along two rods is compared with the experimental results. Models such as the $k-\epsilon$ and RST with Xu two-layer formulation have a better agreement with the experiment. The Wolfstein formulation specifically used in shear driven flows has over predicted the temperatures. Other models have also significantly over predicted the temperature distribution. This may be due to lower convection and/or turbulent diffusion near-wall. Comparing the turbulent viscosity ratios of the two-layer models may provide answers to this. There is negligible difference in temperature distribution for the standard $k-\epsilon$ and realizable $k-\epsilon$ models, hence only the realizable is presented here as this model predicts flow rate closer to experimental data.

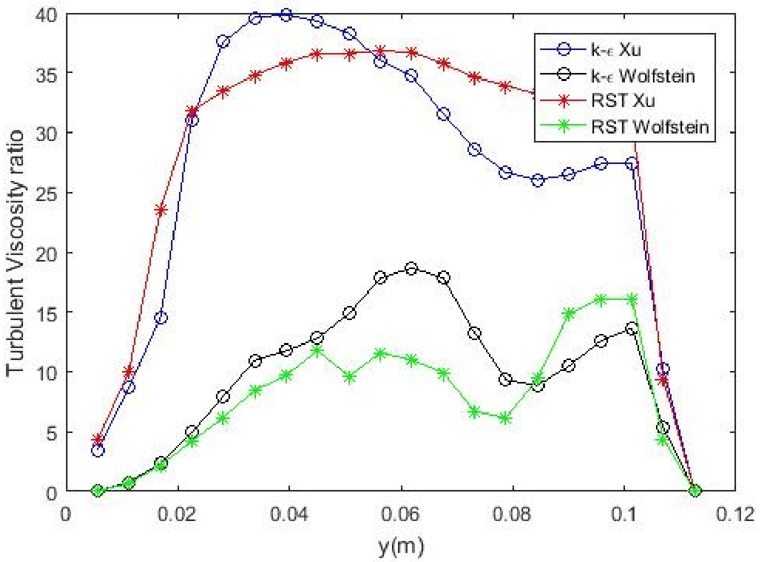

Fig. 4.2: Axial variation of turbulent viscosity ratio.

Shown in Fig. 4.2 is a comparison of the turbulent viscosity ratios for the two two-layer formulations using both the $k-\epsilon$ and RST turbulence models. The plot is a graph of turbulent viscosity plotted along a straight line from the periphery of the rod to the edge of the domain. The plots have a direct correlation with the temperature distribution. The Xu formulation has a higher turbulent viscosity ratio; hence, a higher effective thermal conductivity. Less thermal resistance in the boundary layer leads to lower rod wall temperatures. The Wolfstein formulation has much lower turbulent viscosity ratio; therefore, the rod wall temperature is higher. Comparing the $k-\epsilon$ and RST model with Xu near-wall formulation, the $k-\epsilon$ has a slightly higher turbulent viscosity ratio; therefore, from Fig. 4.1 it is noticeable that the $k-\epsilon$ model predicts slightly lower rod wall temperature compared to the RST model with Xu formulation. When a similar comparison is made with Wolfstein formulation it can be seen that the $k-\epsilon$ model again seems to predict a slightly lower rod wall temperature, which is also due to the difference in turbulent viscosity ratios. It is clear that the Xu near-wall formulation is well suited for natural convection flows.

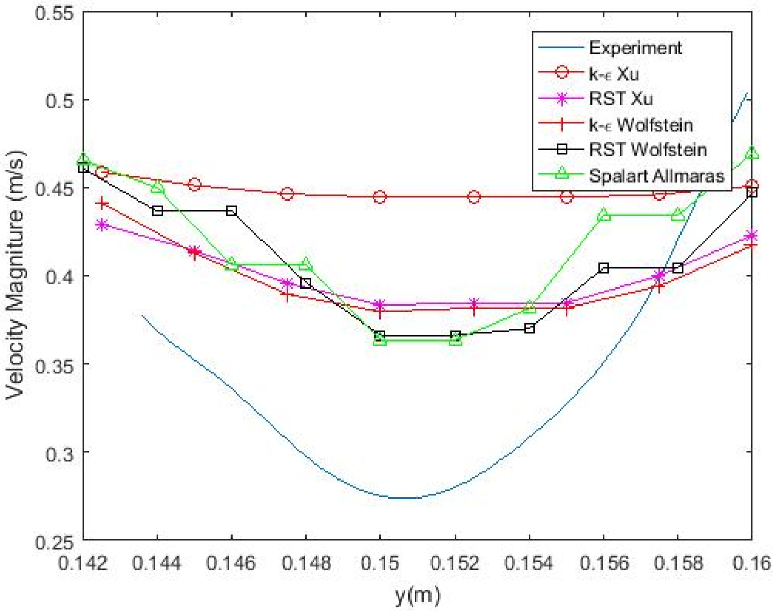

Fig. 4.3: Experimental vs. CFD velocity profile at x=0.0m, z=0.476m, 700 W/m^2.

The velocity profiles are plotted at eight different regions of the domain corresponding to the experiment in the wake region between the rods. Shown in Fig. 4.3 is a plot of the velocity profiles at x=0.0m and z=0.476m. There is clearly no correspondence here with the experimental data, although some trends can be observed in some of the turbulence models, they are not significant. Similar inferences can be made from Fig. 4.4 and Fig.

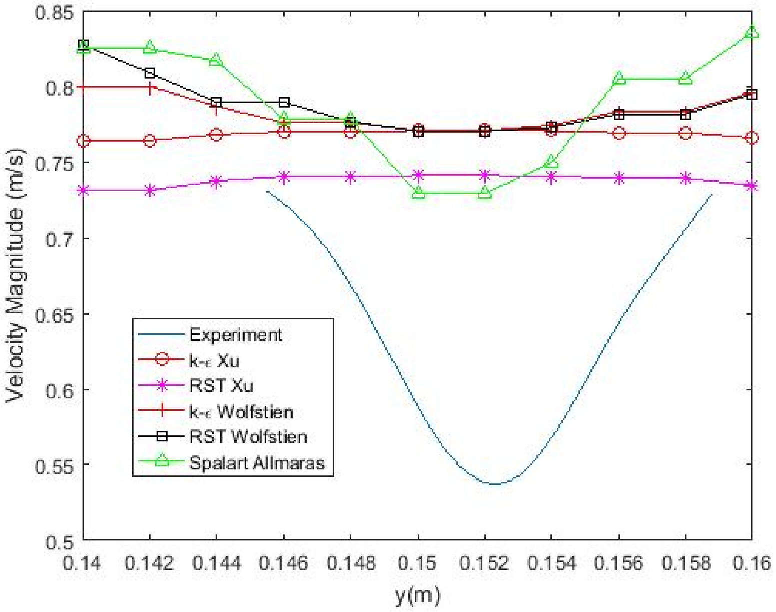

Fig. 4.4: Experimental vs. CFD velocity profile at x=0.0m, z=0.825m, 700 W/m^2.

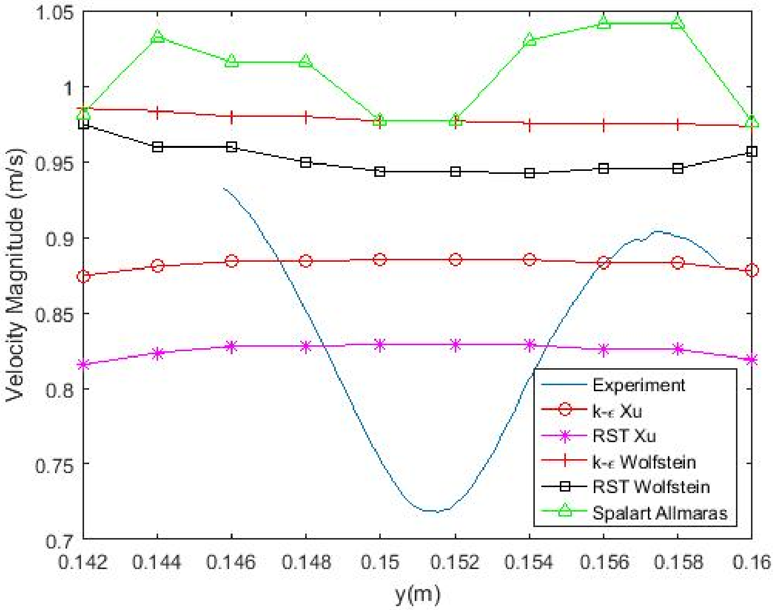

Fig. 4.5: Experimental vs. CFD velocity profile at x=0.0m, z=1.174m, 700 W/m^2.

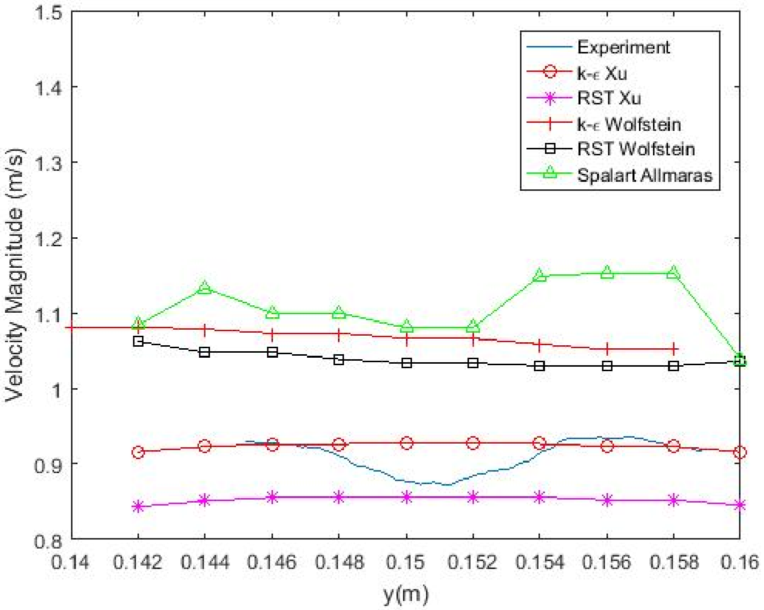

Fig. 4.6: Experimental vs. CFD velocity profile at x=0.0m, z=1.524m, 700 W/m^2.

4.5. Although from Fig. 4.6 it can be seen that the $k-\epsilon$ Xu formulation model has some modest agreement with the experimental data. Towards the center, at y=0.15m it fails to correspond, perhaps due to inadequate mesh resolution. Other models have significantly over-predicted or under-predicted the velocities.

From Fig. 4.7, the velocity profile at x=-0.06m, z=0.476m, reveals that some of the turbulence models have been able to establish a similar trend with that of the experimental data. It must be noted that the RST models with Xu formulation show the strongest agreement with the experiment. This is established by the presence of two values at y=0.15m in the domain which are very close to the experimental data. The $k-\epsilon$ models have failed to show any agreement at this location.

From Fig. 4.8 the turbulence models may seem to establish a velocity trend but there is no strong correlation with the experiment. Similarly, from Fig. 4.9 such inference can also be made. Albeit, Spalart-Allmaras seems to show stronger trend than the other models. From Fig. 4.10 it can be observed that although some of the turbulence models again

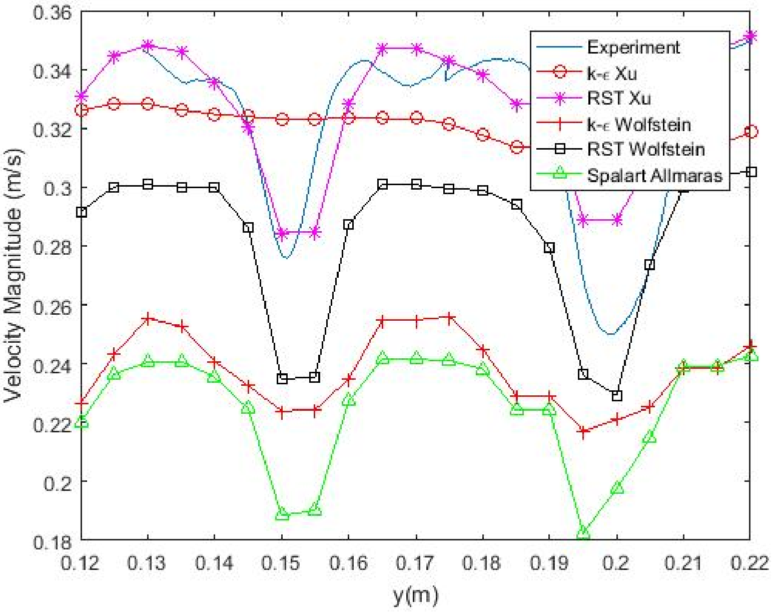

Fig. 4.7: Experimental vs. CFD velocity profile at x=-0.06m, z=0.476m, 700 W/m^2.

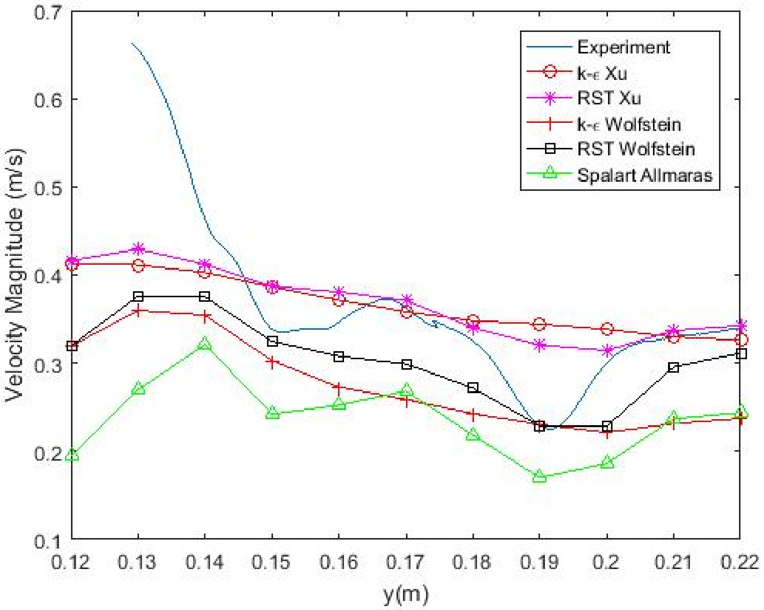

Fig. 4.8: Experimental vs. CFD velocity profile at x=-0.06m, z=0.825m, 700 W/m^2.

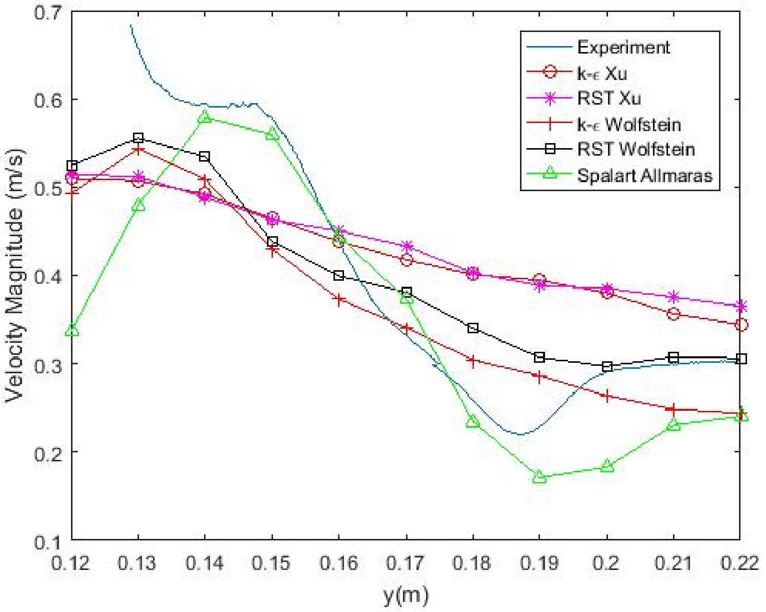

Fig. 4.9: Experimental vs. CFD velocity profile at x=-0.06m, z=1.174m, 700 W/m^2.

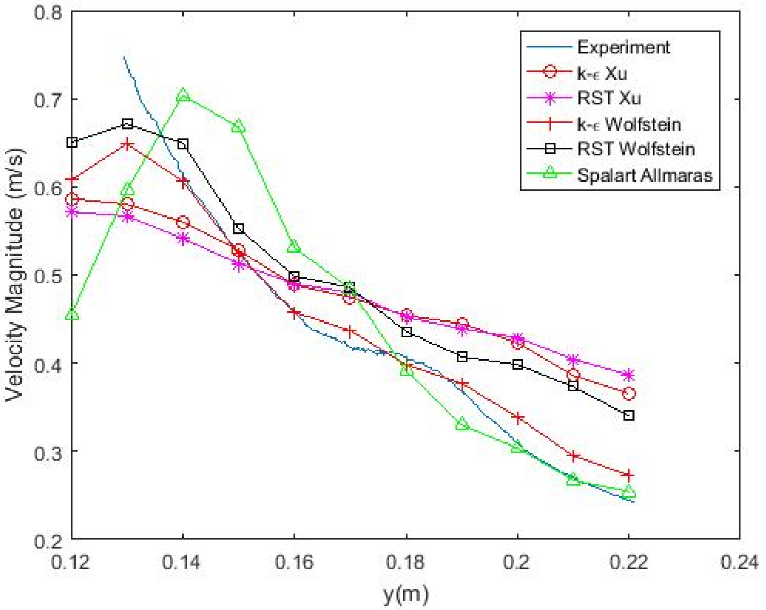

Fig. 4.10: Experimental vs. CFD velocity profile at x=-0.06m, z=1.524m, 700 W/m^2.

establish some trend with the experimental results, the $k-\epsilon$ model with Wolfstein near-wall formulation seems to have a stronger correlation with the experimental data.

None of the turbulence model velocity profile seems to strongly correlate with the experimental data at all eight locations. Some perform better than others at different locations. The RST models seems to be slightly better than the other turbulence models when it comes to correlating velocity profiles. It must also be taken into account that these locations are present in the wake regions behind the grid spacers. The relative low mesh resolutions in the wake regions may have caused such disparity between the experimental and CFD results. The cell count in the domain is 8 million and to resolve the wake region with higher mesh resolution is currently beyond practical bounds.

A contour plot of velocity is plotted on y=0.0 plane along the streamwise direction. The plots presented here represent the turbulence models that have been able to accurately predict the experimental results, notably the $k-\epsilon$ and RST turbulence models with Xu near-wall formulation. Comparing the contour plots of velocity, the $k-\epsilon$ model predicts a slightly higher velocity in the plume region downstream than does the RST model. The temperature contour plot for the mentioned two turbulence models has about $1.5K$ temperature difference between them globally. Overall, there is a negligible difference between the contour plots obtained from the two turbulence models.

4.2 400 W/m^2 Case

Only two turbulence models are studied for the 400 W/m^2 case; the $k-\epsilon$ and RST, both with Xu near-wall formulation. From the 700 W/m^2 case, it is clear that these two turbulence models are able to predict solutions closest to the experimental results. In this section, flow rate, the temperature distribution on the rods, as well as velocity profiles at 8 locations are presented. Contour plots of velocity and temperature along the stream wise direction are also presented.

From Table 4.2, the flow rate for the two models is reasonably close to the experimental result. The percentage error in CFD results is around 5 percent, which is within the acceptable range. The loss coefficient of $K = 286$ specified at inlet has resulted in an accurate

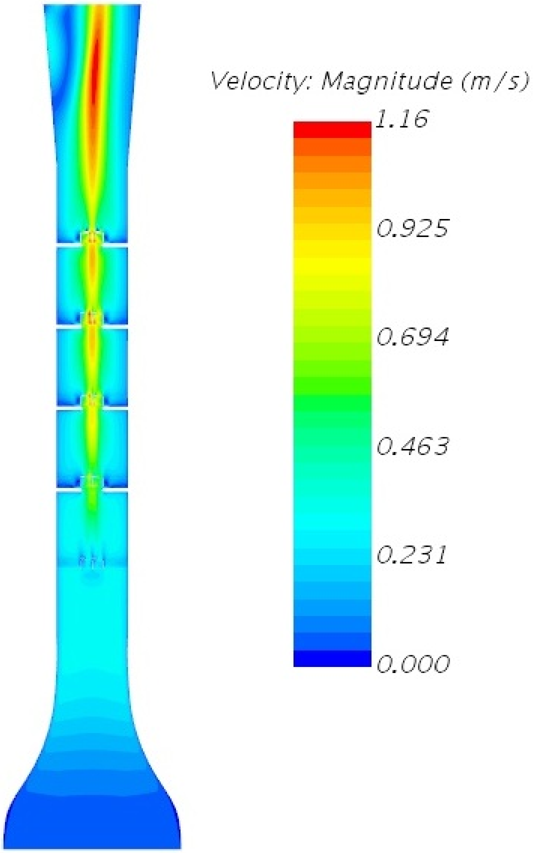

Fig. 4.11: Contour plot of velocity for $k-\epsilon$ Xu model; 700 W/m^2.

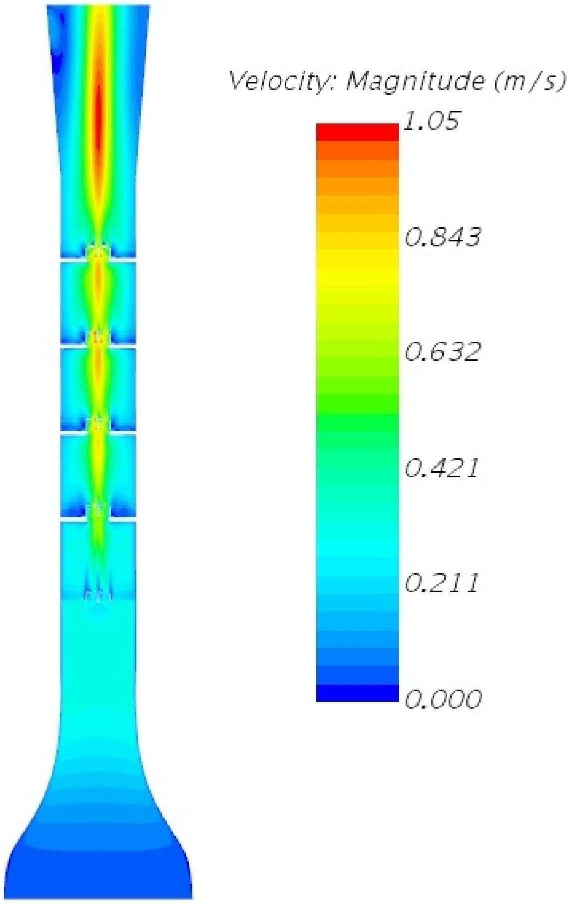

Fig. 4.12: Contour plot of velocity for RST Xu model; 700 W/m^2.

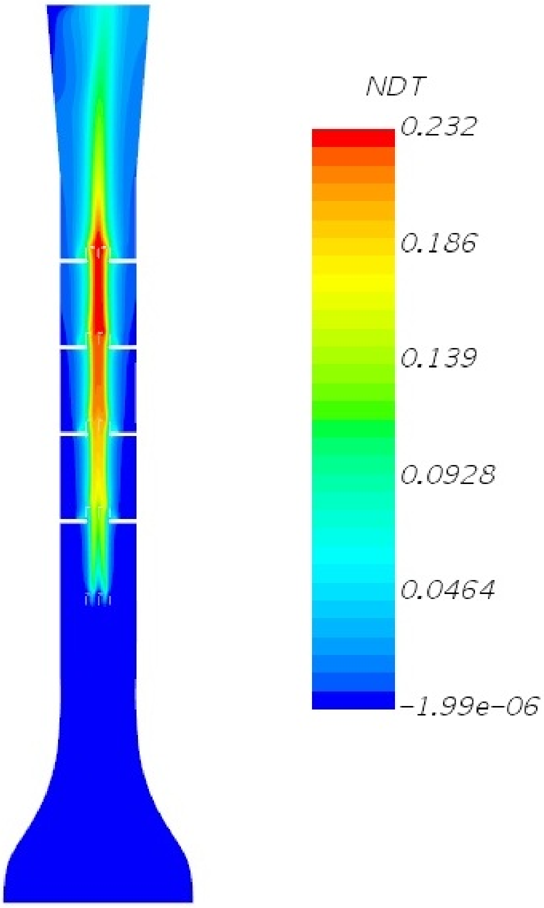

Fig. 4.13: Contour plot of normalized temperature for $k-\epsilon$ Xu model; 700 W/m^2.

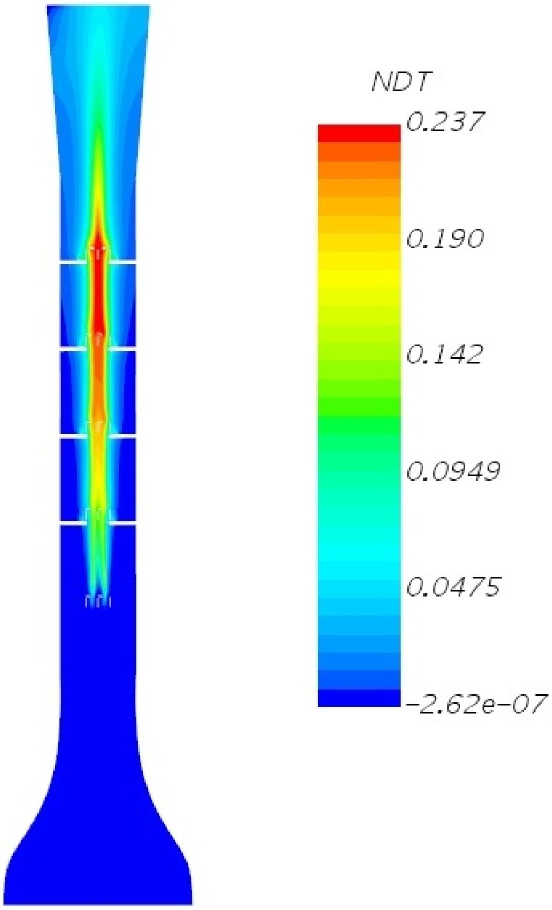

Fig. 4.14: Contour plot of normalized temperature for RST Xu model; 700 W/m^2.

reduction of flow rate across the domain.

Fig. 4.15 is a plot of the temperature distribution. It can be seen that both the models have been able to predict the distribution with good accuracy. A closer look at the temperature distribution for rod 1 and rod 2 for the RST Xu model suggests that there is a change in distribution which is more than that of $k-\epsilon$ with Xu near-wall formulation. This may be due to the presence of the swirling elements on the grid spacers. As anticipated, the two-layer formulation of Xu has repeatedly shown good correlation with experimental data.

The velocity profiles are located exactly as in the case of 700 W/m^2. Figures 4.16, 4.17, 4.18, and 4.19 show velocity profiles at locations $x = 0.0$m and $z = 0.474$m, 0.825m, 1.174m,

Table 4.2: Flow rates for 400 W/m^2 case.

Turbulence Model	CFD kg/s	Exp kg/s
Realizable $k-\epsilon$, Xu	0.0201	0.019
RSM, Xu	0.0208	0.019

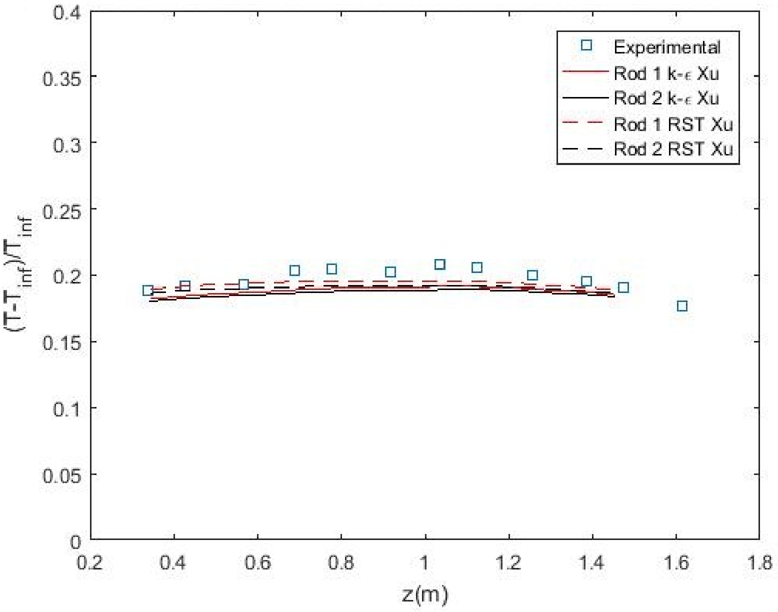

Fig. 4.15: Temperature distribution on rods with two turbulence models for the 400 W/m^2.

and 1.524m, respectively. As expected, there is no strong correlation with the experimental data at these locations perhaps due to inadequate grid resolution.

Figures 4.20, 4.21, 4.22, and 4.23 show velocity profiles at locations x = -0.06m and z = 0.474m, 0.825m, 1.174m, and 1.524m, respectively. The results have improved in comparison to results at location x=0.0m. The notable velocity profile is the RST Xu model in Fig. 4.20, where a similar pattern is observed with the 700 W/m^2 case. The profiles at other locations do not exhibit strong agreement with experimental data.

Contour plots of velocity and temperature are plotted along streamwise direction on x=0.0 plane. The $k-\epsilon$ model predicts slightly higher velocity in comparison to RST. The temperature profiles have little or no difference in general with $1K$ differences globally.

From both the cases, it can be inferred that difference in the heat flux boundary condition affects the velocity magnitude. This is no surprise as a higher temperature gradient

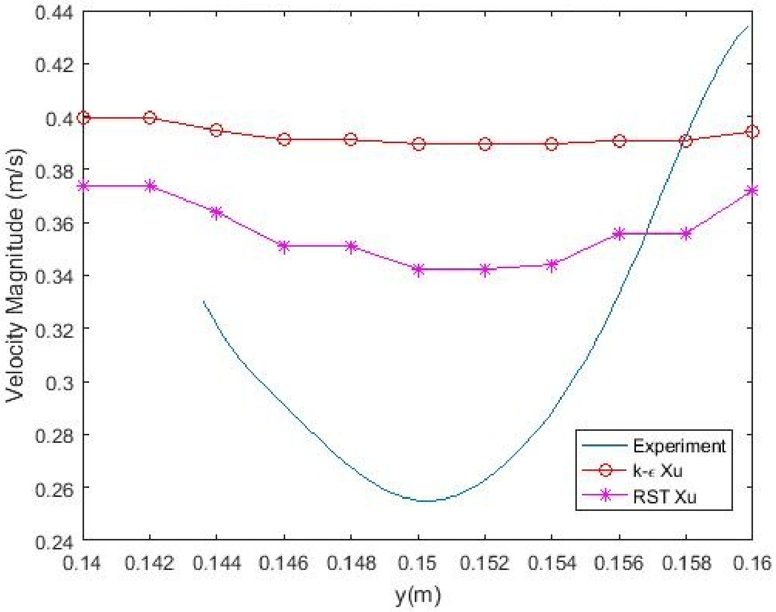

Fig. 4.16: Experimental vs. CFD velocity profile at x=0.0m, z=0.476m, 400 W/m^2.

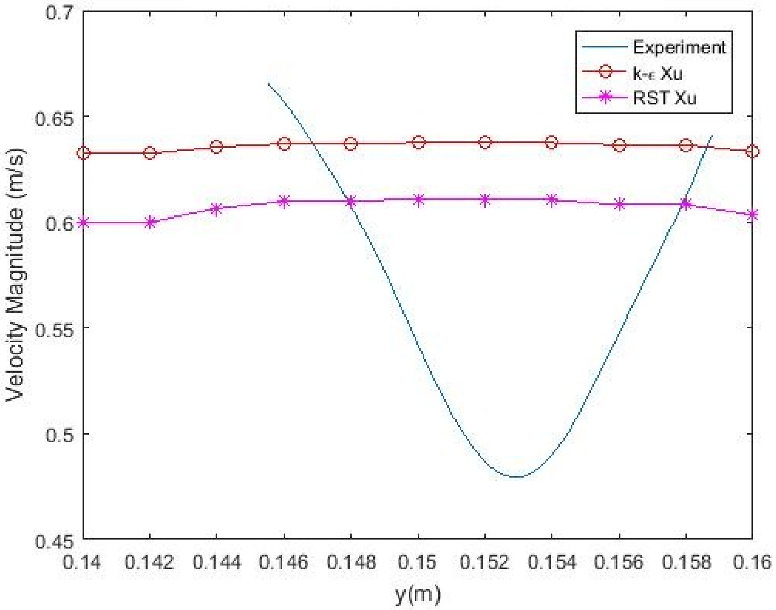

Fig. 4.17: Experimental vs. CFD velocity profile at x=0.0m, z=0.825m, 400 W/m^2.

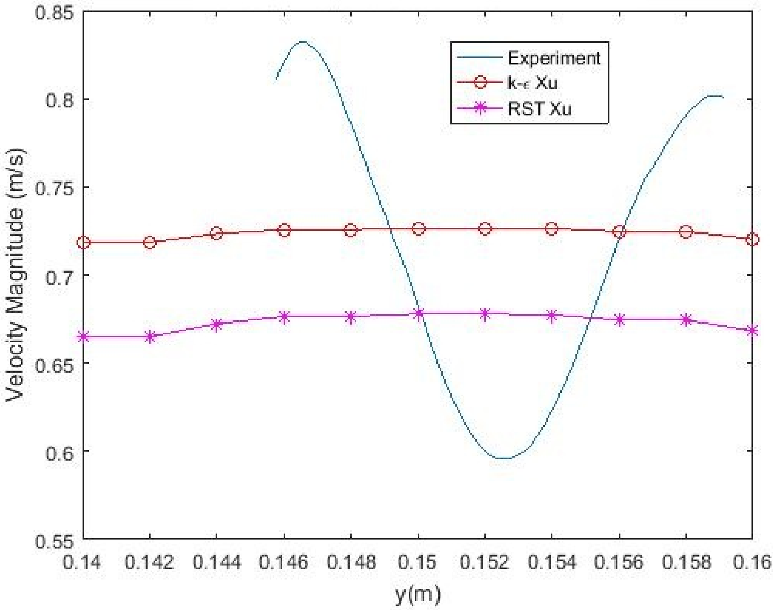

Fig. 4.18: Experimental vs. CFD velocity profile at x=0.0m, z=1.174m, 400 W/m^2.

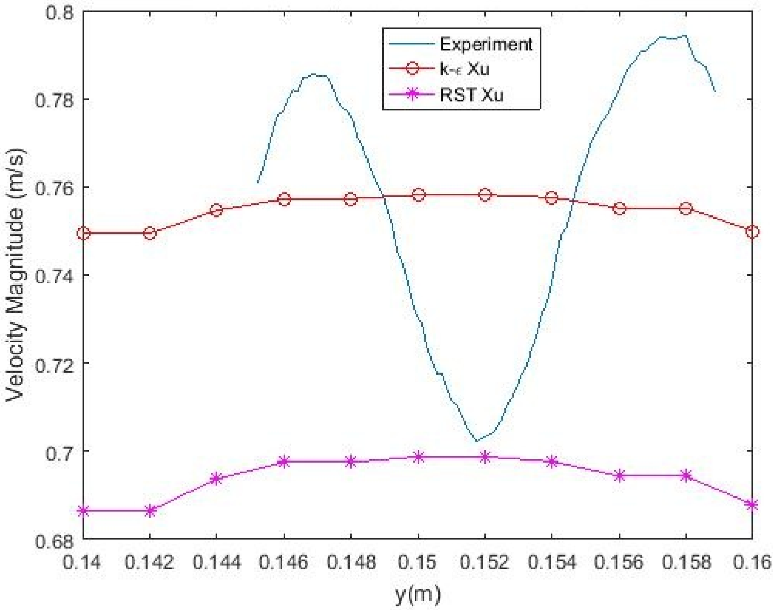

Fig. 4.19: Experimental vs. CFD velocity profile at x=0.0m, z=1.524m, 400 W/m^2.

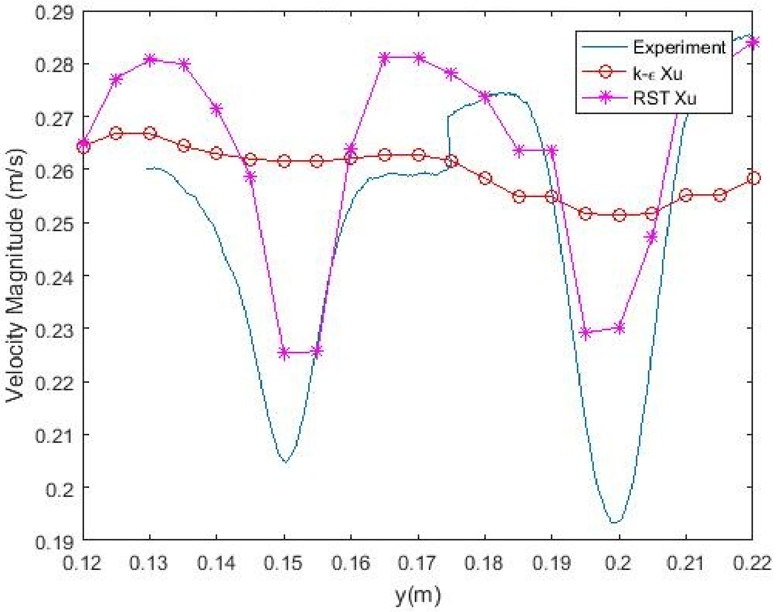

Fig. 4.20: Experimental vs. CFD velocity profile at x=-0.06m, z=0.476m, 400 W/m^2.

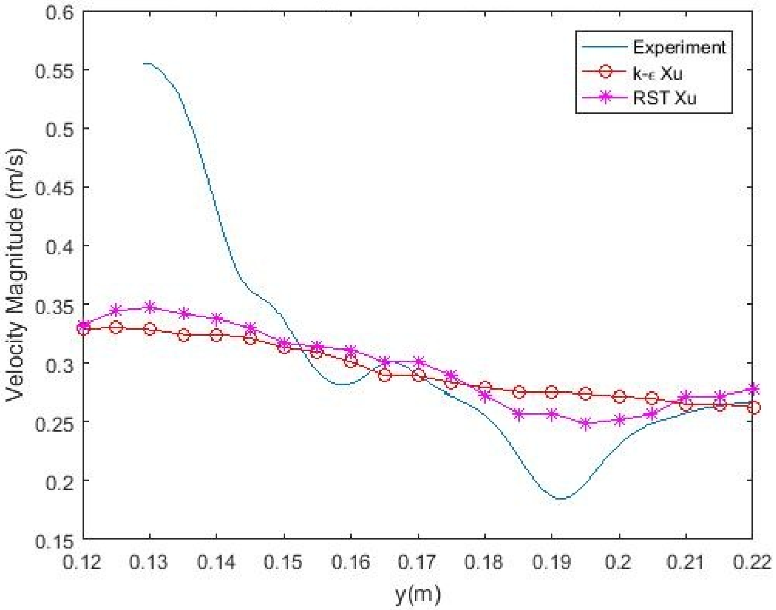

Fig. 4.21: Experimental vs. CFD velocity profile at x=-0.06m, z=0.825m, 400 W/m^2.

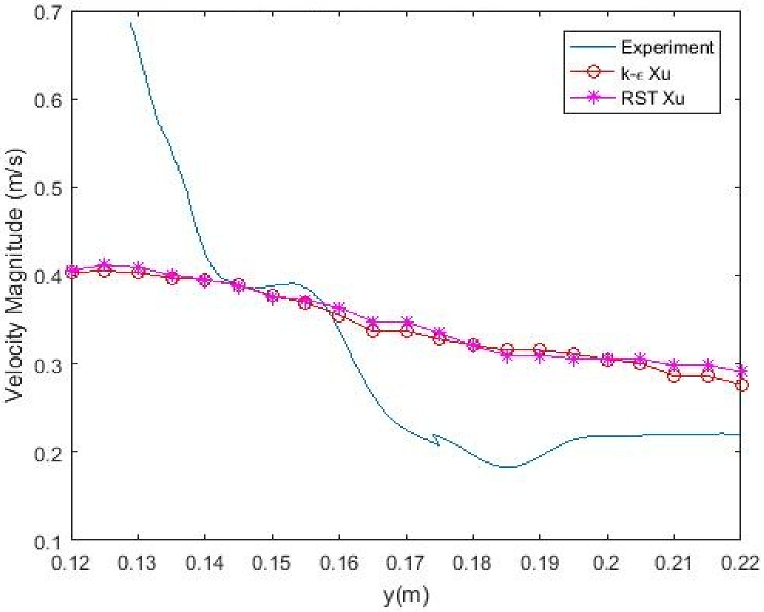

Fig. 4.22: Experimental vs. CFD velocity profile at x=-0.06m, z=1.174m, 400 W/m^2.

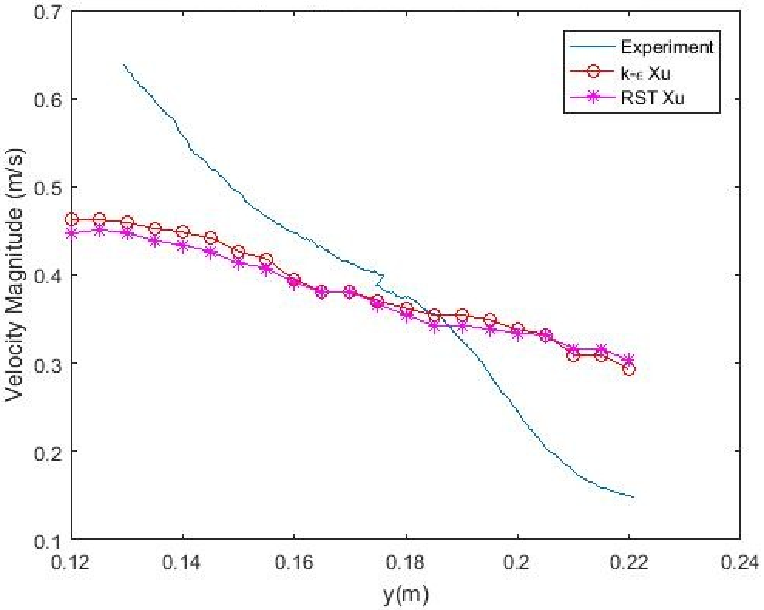

Fig. 4.23: Experimental vs. CFD velocity profile at x=-0.06m, z=1.524m, 400 W/m^2.

must create higher density differences in the near-wall region of the heat transfer surface; therefore, higher velocities result. Even though there is an obvious difference in velocity magnitude, there seems to be some patterns observed in both the cases, for example from Fig. 4.7 and Fig. 4.20. However, both the cases have no strong correlation with the experimental results when comparing velocity profiles. Having said this, the $k-\epsilon$ and RST model with Xu formulation do accurately predict the temperature distribution for both cases, as well as the mass flow rate.

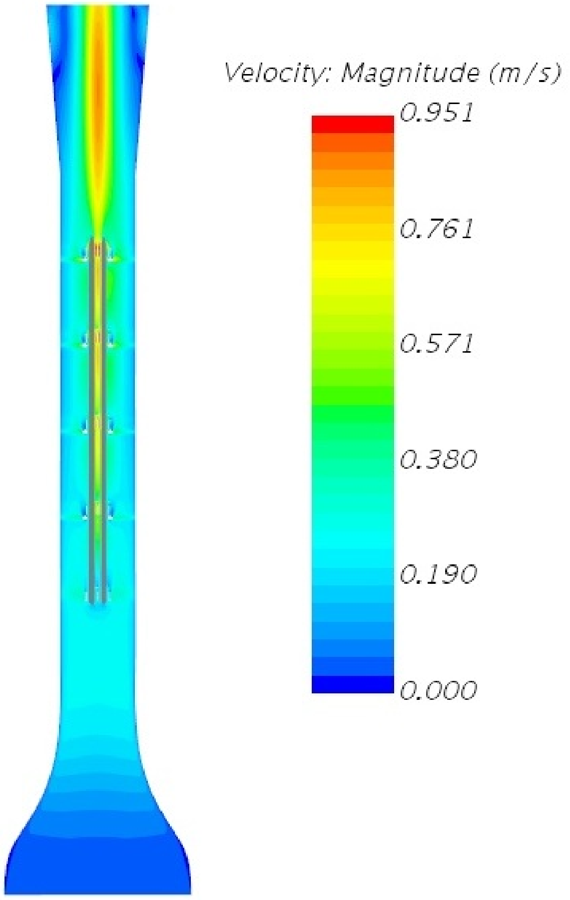

Fig. 4.24: Contour plot of velocity for $k-\epsilon$ Xu model; 400 W/m^2.

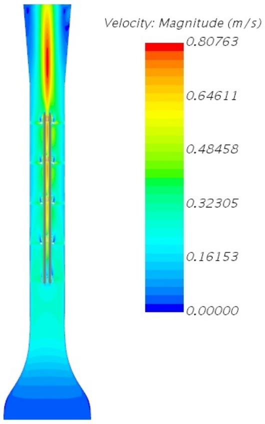

Fig. 4.25: Contour plot of velocity for RST Xu model; 400 W/m^2.

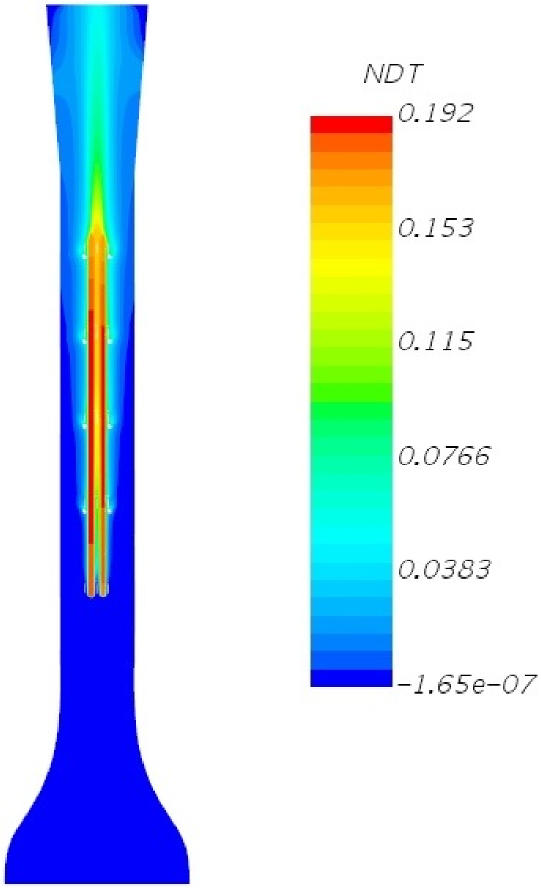

Fig. 4.26: Contour plot of normalized temperature for $k-\epsilon$ Xu model; 400 W/m^2.

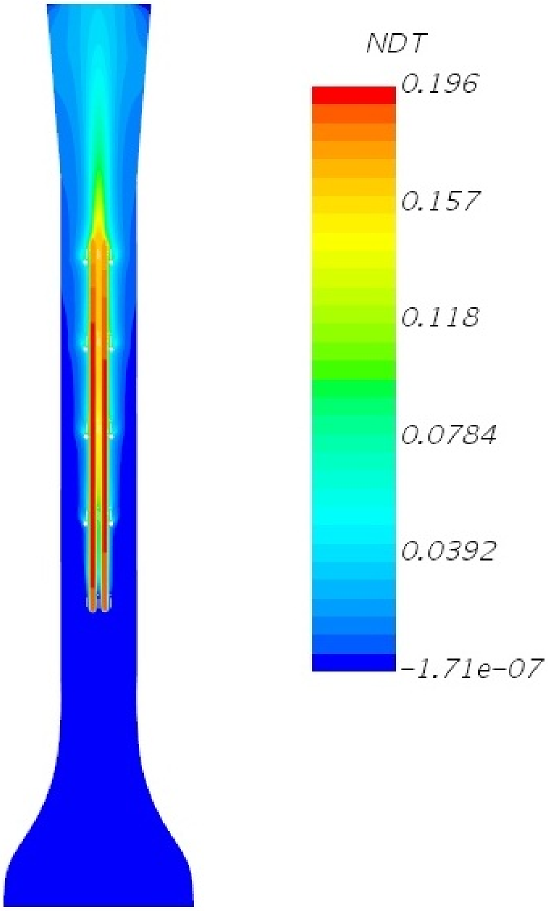

Fig. 4.27: Contour plot of normalized temperature for RST Xu model; 400 W/m^2.

4.3 Grid Independence Study

Even though the solutions for flow rates and temperature distributions are accurate, there may be discretization error due to inadequate cell resolution in the domain. For a solution to achieve grid independence the solution must remain relatively unchanged with systematic reduction in cell size (i.e. increase in cell count).

The 700 W/m^2 case is chosen for this study. Cell counts of 4, 8, and 16 million are used. Since the only change in both cases are the heat flux boundary conditions and pressure loss coefficients, grid independent study for one case will be sufficient. This study includes flow rates and temperature distribution for the $k-\epsilon$ and RST with Xu near-wall formulation.

Table 4.3: Flow rate: grid independence study for $k-\epsilon$ Xu turbulence model.

Cell Count	CFD kg/s
4 million	0.0266
8 million	0.0257
16 million	0.0267

The results from Table 4.3 for the $k-\epsilon$ suggest that there is no significant change in mass flow rate. The consequent results are with an error margin of 3 percent.

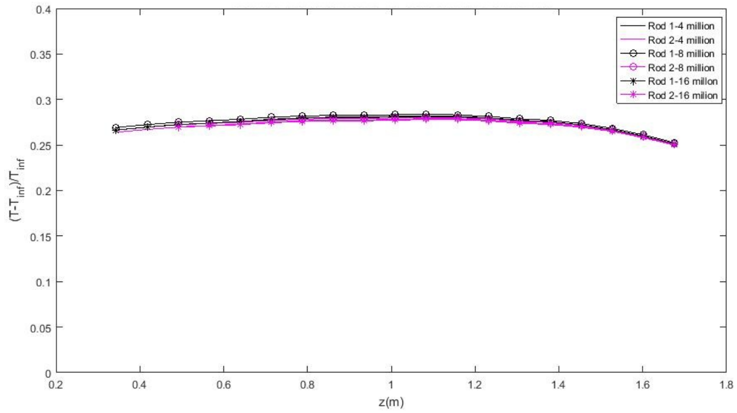

Fig. 4.28: Temperature distribution: grid independent study for $k-\epsilon$ Xu turbulence model.

The temperature distribution shown in Fig. 4.28 reveal no noticeable difference in results with increase in cell count. Based on the results from Table 4.3 and Fig. 4.28 it can be concluded that the solution for wall temperature using $k-\epsilon$ turbulence model with Xu formulation is essentially grid independent.

Table 4.4: Flow rate: grid independence study for RST Xu turbulence model.

Cell Count	CFD kg/s
4 million	0.0287
8 million	0.0273
16 million	0.0278

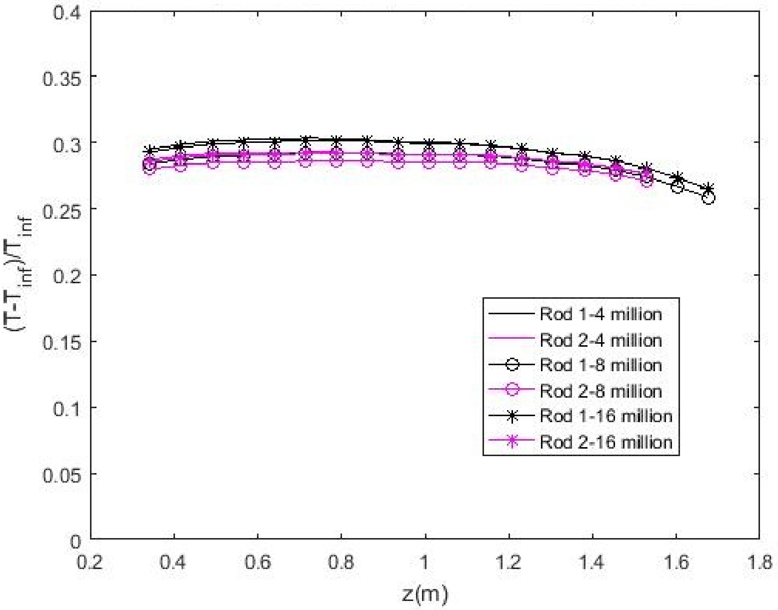

Fig. 4.29: Temperature distribution :grid independence study for $k-\epsilon$ Xu turbulence model.

From Table 4.4, it can be observed that the flow rates computed using the RST model have little difference with an error of 3 percent. Temperature distribution shown in Fig. 4.29 also suggest negligible change in results.

From the grid independent study it can be concluded that the solutions for flow rate and rod wall temperature are sufficiently grid independent for both the $k-\epsilon$ and RST turbulence models with Xu near-wall formulation and that the solution from the intermediate mesh size of 8 million is acceptable.

CHAPTER 5

CONCLUSION

Numerical modeling of natural convection in vertically heated rods is performed. The turbulence is modeled using the steady Reynolds-averaged Navier-Stokes equation. Five different turbulence models are chosen; namely, standard and realizable $k-\epsilon$, Reynolds stress transport, Spalart-Allmaras, and standard $k-\omega$. In addition, Xu (buoyancy driven), and Wolfstein (shear driven) two-layer near-wall formulations are employed along with $k-\epsilon$ and RST models. The interpolation schemes used are second-order upwinding for convective terms and second-order central differencing for diffusion terms. The pressure velocity coupling is done using the SIMPLE method. Two cases with different heat flux boundary conditions are studied, 700 W/m^2 and 400 W/m^2. The solutions are compared with experimental studies conducted by Jones [1].

The realizable $k-\epsilon$ and RST model with Xu near-wall formulation have strongest correlation with the temperature distribution and flow rates of the experiment. The Wolfstein two-layer formulation does not perform as well as the Xu formulation, notably because Xu formulation produces a higher near-wall turbulent viscosity ratio than Wolfstein with an increase in the thermal diffusion. Also, the Xu formulation is specifically designed for buoyancy driven flows. The Spalart-Allmaras model also failed to correlate well with the temperature distribution and mass flow rate results from experiment.

It can be concluded that none of the turbulence models were able to accurately predict the velocity profiles at various location for both cases. Notably, the RST model with Xu near-wall formulation is better than the other models at some of the locations. The $k-\omega$ turbulence model has failed to converge. The Spalart-Allmaras model exhibited weak correlation with the experimental results. The disparity in velocity profiles may also be likely due to inadequate mesh resolution in the wake region behind the grid spacers. With the currently available computational resources a higher resolution is not practical. Large eddy simulations or detached large eddy simulations may be able to accurately capture the physics in the wake region since both the models require high fidelity mesh resolution, but this is currently not within the scope of the study.

However, the realizable $k - \epsilon$ and RST turbulence models with Xu formulation, were able to accurately predict the flow rates as well as the temperature distributions, even though the velocity profiles have a weak correlation with the experimental results at the various locations. Further, the Xu near-wall formulation has repeatedly shown to have good agreement with the experimental data. Hence, it is concluded that for flows involving buoyancy the Xu near-wall formulation is well suited.

REFERENCES

[1] Jones, K. L., *Benchmark Experiments for Natural Convection in Nuclear Fuel Rods Bundles*, Ph.D. thesis, Utah State University, 2016.

[2] Nusselt, W., "Die verbrennung und die vergasung der kohle auf dem rost," *International Journal of Heat and Mass Transfer*.

[3] Ackermann, G., *Die wrmeabgabe eines horizontalen geheizten rohres an kaltes wasser bei natrlicher konvektion*, 1938, pp. 40–51.

[4] Morgan, V. T., *The overall convective heat transfer from smooth circular cylinder*, 1975, pp. 100–268.

[5] Churchill, S. W. and Chu, S. S., "Correlating equations for laminar and turbulent free convection from horizontal cylinder," 1975, pp. 1049–1053.

[6] Kuehn, T. H. and Goldestine, R. J., "Numerical solutions to Navier-Stokes equations for laminar natural convection about a horizontal isothermal circular cylinder," 1908.

[7] Farouk, B. and Guceri, S. I., "Natural convection from horizontal cylinder-laminar regime," 1981, pp. 522–527.

[8] T Saitoh, T Sajiki, K. M., "Bench Mark solutions to natural convection heat transfer problem around a horizontal circular cylinder," 1993, pp. 1251–1259.

[9] Cesini, G., "Natural convection from a horizontal cylinder in a rectangular cavity," 1999, pp. 1801–1811.

[10] K Kitamura, F Kami-iwa, T. M., "Heat transfer and fluid flow of natural convection around large horizontal cylinders," 1999, pp. 4093–4106.

[11] J Lieberman, B. G., "Interactions in natural convection from an array of heated elements, experimental," 1969, pp. 1385–1396.

[12] Marsters, G. F., "Array of heater horizontal cylinder in natural convection," 1972, pp. 921–933.

[13] M Ashjaee, T. Y., "Experimental study of natural convection heat transfer from vertical array of isothermal horizontall elliptical cylinders," 2007, pp. 240–248.

[14] W M sparrow, J. E. N., "Effect of vertical separation distance and cylinder-to-cylinder temperature imbalance on natural convection for a pair of horizontal cylinders," 1981, pp. 638–644.

[15] Ghasemi, S. M. A. B., "Natural convection cooling of a localised heat source at the bottom of a nanofluid-filled enclosure," 2009, pp. 630–640.

[16] Xiangyin Meng, Y. L., "Numerical study of natural convection in a horizontal cylinder filled with water based alumina nanofluid," 2015, pp. 3–9.

[17] CD-adapco, "STAR-CCM+ ,Version 11.040," 2016.

[18] Rodi, W., "Experience with Two-Layer Models Combining the k-e Model with a One-equation Model Near the wall," *29th Aerospace Science Meething*.

[19] W Xu, Q. C. and Nieuwastadt, F. T. N., "A New Turbulence model for Near-Wall Convection," *International Journal of Heat and Mass transfer*, 1998, pp. 3161–3176.

[20] Wolfstein, M., "The Velocity and Temperature Distribution in a One-Dimensional Flow with Turbulence Augmentation and Pressure Gradient," *International Journal of Heat and Mass transfer*, 1969, pp. 301–318.

[21] Spalart, P. R. and Allmaras, S. R., "A One-Equation Turbulence Model for Aerodynamics Flows," *AIAA paper*.

[22] Jones, W. and Launder, B., "The prediction of laminirization with a two equation model of turbulence," *International Journal of Heat and Mass transfer*, 1972, pp. 301–314.

[23] Chen, C.-J. and Jaw, S.-Y., *Fundamentals of Turbulence Modeling*, 1989, pp. 21–59.

[24] T Shin, W Liou, A. S. Z. Y. and Zhu, J., "New $k - \epsilon$ Eddy Viscosity Model for High Reynolds Number Turbulent flows," *Computers and Fluids*.

[25] Saffman, P., "A Model for Inhomogeneous Turbulent Flow," *Proc.R.Society London*.

[26] B Launders, D. S., *Lectures in Mathematical Models of Turbulence*.

[27] Wilcox, D., *Turbulence Modeling for CFD,* 2^{nd} *Ed*.

[28] Launders, B. E., "Second Moment Cosure: Present.. and future?" *International Journal of Heat and Fluid Flow*.

[29] B E Launders, N. S., "Second Moment Closure for the Near-Wall Sublayer: Development and Application," *AIAA J*.